

# Orientation-Aware 3D SLAM in Alternating Magnetic Field from Powerlines

RONGRONG WANG<sup>✉\*</sup>, Singtel Cognitive and AI Lab for Enterprises, Nanyang Technological University, Singapore

RUI TAN<sup>✉\*</sup>, Singtel Cognitive and AI Lab for Enterprises, Nanyang Technological University, Singapore

ZHENYU YAN<sup>✉†</sup>, Department of Information Engineering, The Chinese University of Hong Kong, China

CHRIS XIAOXUAN LU<sup>✉</sup>, School of Informatics, University of Edinburgh, UK

Identifying new sensing modalities for indoor localization is an interest of research. This paper studies powerline-induced alternating magnetic field (AMF) that fills the indoor space for the orientation-aware three-dimensional (3D) simultaneous localization and mapping (SLAM). While an existing study has adopted a uniaxial AMF sensor for SLAM in a plane surface, the design falls short of addressing the vector field nature of AMF and is therefore susceptible to sensor orientation variations. Moreover, although the higher spatial variability of AMF in comparison with indoor geomagnetism promotes location sensing resolution, extra SLAM algorithm designs are needed to achieve robustness to trajectory deviations from the constructed map. To address the above issues, we design a new triaxial AMF sensor and a new SLAM algorithm that constructs a 3D AMF intensity map regularized and augmented by a Gaussian process. The triaxial sensor's orientation estimation is free of the error accumulation problem faced by inertial sensing. From extensive evaluation in eight indoor environments, our AMF-based 3D SLAM achieves sub-1m to 3m median localization errors in spaces of up to 500 m<sup>2</sup>, sub-2° mean error in orientation sensing, and outperforms the SLAM systems based on Wi-Fi, geomagnetism, and uniaxial AMF by more than 30%.

**CCS Concepts:** • Human-centered computing → Ubiquitous and mobile computing systems and tools; • Computer systems organization → Sensors and actuators.

Additional Key Words and Phrases: Electromagnetic radiation, Powerline network, Simultaneous localization and mapping, Indoor localization

## ACM Reference Format:

Rongrong Wang<sup>✉</sup>, Rui Tan<sup>✉</sup>, Zhenyu Yan<sup>✉</sup>, and Chris Xiaoxuan Lu<sup>✉</sup>. 2023. Orientation-Aware 3D SLAM in Alternating Magnetic Field from Powerlines. *Proc. ACM Interact. Mob. Wearable Ubiquitous Technol.* 7, 4, Article 182 (December 2023), 26 pages. <https://doi.org/10.1145/3631446>

## 1 INTRODUCTION

Simultaneous localization and mapping (SLAM) is the task of constructing a map of an unknown environment using a mobile device's measurement trace while simultaneously keeping track of the mobile's location within the environment. Recent SLAM systems adopt the GraphSLAM formulation [14] that integrates odometry and a

\* Also with School of Computer Science and Engineering, Nanyang Technological University, Singapore.

† Part of this work was completed while Zhenyu Yan was with Singtel Cognitive and Artificial Intelligence Lab for Enterprises, Nanyang Technological University, Singapore.

Authors' addresses: Rongrong Wang<sup>✉</sup>, rrwang@ntu.edu.sg, Singtel Cognitive and AI Lab for Enterprises, Nanyang Technological University, Singapore; Rui Tan<sup>✉</sup>, Singtel Cognitive and AI Lab for Enterprises, Nanyang Technological University, Singapore, ruitan@ntu.edu.sg; Zhenyu Yan<sup>✉</sup>, zyyan@ie.cuhk.edu.hk, Department of Information Engineering, The Chinese University of Hong Kong, China; Chris Xiaoxuan Lu<sup>✉</sup>, School of Informatics, University of Edinburgh, UK, xiaoxuan.lu@ed.ac.uk.

Permission to make digital or hard copies of part or all of this work for personal or classroom use is granted without fee provided that copies are not made or distributed for profit or commercial advantage and that copies bear this notice and the full citation on the first page. Copyrights for third-party components of this work must be honored. For all other uses, contact the owner/author(s).

© 2023 Copyright held by the owner/author(s).

2474-9567/2023/12-ART182

<https://doi.org/10.1145/3631446>

sensing modality producing location-dependent measurements. The performance of SLAM is largely affected by the location discriminability of the used sensing modality. In the last decade, various sensing modalities have been exploited for indoor SLAM, including vision [29], Wi-Fi [1, 13, 23, 46, 50, 54], geomagnetic field (GMF) [22, 51], and lidar [24]. However, these modalities may have reduced location sensing capabilities when their limiting factors take effect. For example, visual sensing suffers from poor illumination; Wi-Fi received signal strength (RSS) can be affected by automatic gain control and multipath fading; Wi-Fi channel state information (CSI)-based sensing [57] requires labor-intensive data collection and labeling as well as high processing capability due to the high-dimensional nature of CSI data; lidar is susceptible to blockage and can be fooled by glass walls. Thus, identifying new sensing modalities for SLAM has been an interest of research.

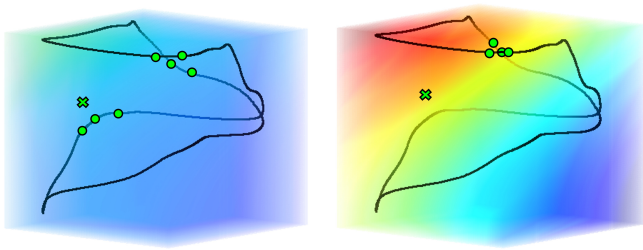
Power distribution networks supplying alternating current (ac) electricity have deeply penetrated into built environments. The currents flowing in the powerlines distributed in the building induce an alternating magnetic field (AMF) that oscillates at the mains frequency (i.e., 50 or 60 Hz). These powerlines include the backbone electricity cables running in the building infrastructure. The AMF can further induce ac noises in the circuits of consumer electronics, which are called *mains hums* and often suppressed by built-in hardware filters. Research has attempted to exploit the mains hum for time-related system functions. The studies [25, 41] design resonant antenna-based sensors to capture the mains hum and exploit its temporal properties, i.e., synchronous periodicity [41] and periodicity imperfection [25], to achieve clock calibration and synchronization. In contrast to exploiting the temporal properties of AMF, this paper aims at exploiting the spatial properties of AMF for SLAM.

AMF is a three-dimensional (3D) vector field. A snapshot of the AMF at a certain time instant can be formally described as  $\vec{F}(\mathbf{x}) \in \mathbb{R}^3$ , where  $\mathbf{x} \in \mathbb{R}^3$  represents a location in the 3D Euclidean space. Essentially, AMF is the sum of the low-frequency magnetic fields induced by all powerlines in the building. Similar to AMF, the GMF and the Wi-Fi infrastructures also provide the respective fields that fill the entire 3D space, which have been exploited for SLAM. As *temporal volatility* and *spatial variability* of the field are important factors for location sensing, we discuss these properties of AMF in comparison with GMF and Wi-Fi. In particular, we focus on the Wi-Fi RSS among Wi-Fi based methods, as it is a more common choice for SLAM systems in practical applications. Note that Wi-Fi RSS has advantages over Wi-Fi CSI in terms of availability from Wi-Fi chip products, implementation complexity and robustness to small dynamics in the environment [17].

First, *temporal volatility* is a destructive factor for location sensing. Due to Wi-Fi's short wavelength, its propagation can be easily affected by the movements of human bodies. Multipath fading makes Wi-Fi RSS volatile. In contrast, AMF is stable over time, because the AMF magnitude at a location is determined by the overall power loading of the building, rather than the operation status of a single appliance unless measured in its proximity. In addition, as AMF is a Super Low Frequency (SLF) source with a very long wavelength, its propagation is not affected by small objects such as human bodies. From our measurements, Wi-Fi RSS's temporal volatility is 7x to 20x higher than AMF.

Second, *spatial variability* is a constructive factor for location sensing. AMF has higher spatial variability than GMF. Indoor GMF is a static vector field perturbed by the building's structural steels, where the perturbations are exploited to learn and infer location information. However, due to the massive scale of the steels, the perturbations offer limited spatial resolutions. As such, GMF-based location sensing can achieve 2m-4m accuracy only. This low discernibility problem can affect the performance of using GMF-based maps for indoor localization [34]. Differently, AMF is induced by powerlines that are sparser in spatial distribution and less bulky in space occupancy compared with the building's structural steels. From our measurements, AMF's spatial variability is more than twice of GMF's.

However, AMF's 3D vector field nature and higher spatial variability present two challenges to the design of a robust AMF SLAM system. **First**, a new triaxial AMF sensor is needed. The existing uniaxial AMF sensor setup used in [25, 41], which suffices for timing, is ill-suited for location sensing. Specifically, the uniaxial



(a) Field with low spatial variability  
(b) Field with high spatial variability

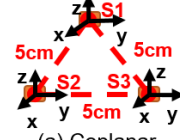
Fig. 1. Higher spatial variability challenges robustness of the map constructed for the movement trajectory only. The cross represents the location of the mobile to be localized; dots represent the in-map locations with the same field intensity value as the mobile, i.e., candidate locations of the in-map localization.



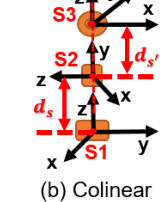
(a) Uni axial



(b) Triaxial



(a) Coplanar



(b) Colinear

Fig. 2. Uni axial and triaxial AMF sensors.  
Fig. 3. Triaxial AMF sensor arrangements.

sensor at location  $\mathbf{x}$  only captures the projection of  $\vec{F}(\mathbf{x})$  onto the axis of the sensor. As a result, the AMF intensity measurement depends on the sensor orientation. Deviation of sensor orientation leads to location sensing errors. Integrating three uniaxial AMF sensors to form a triaxial sensor is a non-trivial task since their physical arrangement highly affects the measurements. In particular, the ac current in the resonant antenna of a uniaxial sensor induced by the AMF for measurement creates a secondary AMF that interferes with the other two uniaxial sensors. The arrangement of three uniaxial sensor components needs to minimize this inter-component interference. This requires conducting design experiments to decide the separation distances of the three resonant antennas. Moreover, the spatial arrangement of the sensor should be simple and compact, making the sensor easily assembled and integrated with the mobile platform for the SLAM and localization tasks. Therefore, properly arranging the three uniaxial sensor components to minimize the inter-component interference while maintaining a satisfactory form factor requires fine considerations and extensive experimentation.

**Second**, AMF's higher spatial variability, although enabling discrimination of closer locations, challenges the robustness of the constructed map. Most SLAM designs only construct the map along the trajectory of the mobile and does not provide an estimate of the signal for a location  $\mathbf{x}'$  in the proximity of the trajectory [1, 11, 30]. While this approach suffices for the fields with low spatial variability (e.g., GMF), it may have degraded performance for fields with high spatial variability (e.g., AMF). In GMF, as the signal at  $\mathbf{x}'$  is similar to that at an in-map location  $\mathbf{x}$  closest to  $\mathbf{x}'$ , the mobile at  $\mathbf{x}'$  during the localization phase can still be localized to an in-map location close to  $\mathbf{x}$ . Differently, in AMF, due to higher spatial variability, the signal at  $\mathbf{x}'$  is more different from that at  $\mathbf{x}$ . As a result, the localization result for the mobile at  $\mathbf{x}'$  is more unpredictable. This is illustrated in Fig. 1, in which the field with high spatial variability suggests candidate locations (represented by solid dots) far away from the mobile's true location (represented by the cross).

To address the above two robustness challenges, in this paper, we make the following two new designs. **First**, we design a *triaxial AMF sensor* that integrates three resonant antennas arranged in three orthogonal orientations. We conduct design experiments to decide the separation distances of the three resonant antennas to avoid mutual interference. As such, the sensor can measure the AMF in three orientations simultaneously. Compared with the uniaxial sensor used in [25, 41], the triaxial sensor's AMF intensity measurement is less susceptible to sensor orientation. **Second**, we employ the Gaussian process (GP) [43] to model AMF and integrate it into GraphSLAM as a regularization term. The GP adopts a kernel function to describe the distance-based prior correlation between

the field intensities at any two locations. With the available AMF intensity measurements on the reconstructed trajectory, the posterior distribution of the AMF intensity at any location out of the trajectory can be updated to have less uncertainty. Localization based on the GP-augmented map is more robust to trajectory deviations.

In addition, as the AMF vector at a certain location is stable over time, we may estimate the orientation variation of the triaxial sensor when it re-visits a location by jointly processing the triaxial readings collected on the original visit and the re-visit. This orientation variation estimation is free of the error accumulation problem faced by the inertial sensing-based odometry.

To evaluate the performance of our AMF-based orientation-aware 3D SLAM system, we use a mobile platform that integrates a wheel-based robot and a six-degree-of-freedom (6DoF) robotic arm to carry the triaxial AMF sensor. We drive the mobile platform to form 3D trajectories with orientation variations in eight indoor environments. We evaluate the mapping and localization accuracy of our system with respect to the known ground-truth trajectories and orientations that are derived from the prescribed movements of the robot and the arm. As baselines, we use the same setup to evaluate the SLAM systems based on Wi-Fi RSS, GMF, and uniaxial AMF sensing without GP regularization and augmentation.

The contributions of this paper include:

- We design a new triaxial AMF sensor and conduct measurements using the sensor to understand the temporal volatility, spatial variability, and orientation property of AMF, in comparison with Wi-Fi RSS and GMF.
- We design AMF-based orientation-aware 3D SLAM that constructs the AMF map in the target 3D space with GP regularization. The AMF intensity map is also augmented with GP to accommodate the deviations of the mobile’s trajectory from the map during the localization phase.
- Evaluation in eight environments shows that our system achieves sub-1m to 3m median localization errors in spaces of up to  $500 \text{ m}^2$ , sub- $2^\circ$  mean error in orientation sensing, and outperforms those based on Wi-Fi RSS, geomagnetism, and uniaxial AMF by more than 30%.

The rest of this paper is organized as follows. §2 reviews related work. §3 presents the design of the triaxial AMF sensor and a measurement study using the designed sensor to understand AMF. §4 presents the design of AMF SLAM. §5 presents experiment results. §7 concludes this paper.

## 2 RELATED WORK

Building’s powerline infrastructure has been exploited for mobile sensing, communication. Powerline communication (PLC) [58] products have been widely available on the market. As mentioned in §1, the studies [25, 41] exploit AMF from powerlines for sensor clock calibration and synchronization. The studies [55, 56] exploit the interactions between powerlines’ low-frequency electrostatic field and human body to achieve clock synchronization and device authentication of wearable devices. A recent study [59] uses the powerline infrastructure as a wired medium to read backscatter tags attached to the walls with powerlines right behind them. The study [38] proposes PLP that uses the power network as antenna to emit modulated wireless signals in two frequencies to localize a mobile receiver. The study [45] extends PLP to use more frequencies to mitigate the aging issue of the location fingerprints captured by the mobile receiver. These two studies [38, 45] apply two power socket plugs to inject the modulated signals into the powerlines and achieve room-level localization. The authors of [27] analyze how PLC systems can be employed to build powerline positioning (PLP) systems. They categorize and discuss three main PLP system architectures depending on whether the system uses specific infrastructure to produce reference positioning signals and whether the target actively collects information to estimate its position. This paper does not employ signal emitters and just uses the low-frequency AMF induced by the powerlines to achieve fine-grained indoor mapping and localization.

The prior work [28] uses a resonate antenna-based uniaxial AMF sensor to design a SLAM system. It achieves mean localization accuracy of 1.59 m in a lab space and 3.93 m in an office building. However, it has the following limitations. First, the uniaxial sensor used in [28] falls short of addressing AMF's nature of 3D vector field. With a uniaxial AMF sensor, the SLAM system is restricted to the scenario where the sensor must be in a fixed orientation when it (re)visits a location. Deviation of sensor orientation can lead to errors of GraphSLAM's loop closure detection during the mapping phase and inaccurate map matching during the localization phase. Second, the design in [28] only constructs the AMF map along the mobile device's movement trajectory. The map does not provide the AMF estimate for any location in the proximity of the trajectory. As discussed in §1, while this design suffices for the fields with lower spatial variability such as GMF, it may have degraded performance for fields with higher spatial variability such as AMF in the presence of trajectory deviations. Differently, this paper does not employ signal emitters and just uses the low-frequency AMF induced by the powerlines to achieve fine-grained indoor mapping and localization. Third, the uniaxial AMF sensor does not have orientation sensing capability. In this paper, we advance the state of the art by designing a new orientation-aware AMF-based 3D SLAM system that addresses AMF's nature of 3D vector field and property of higher spatial variability and provides orientation estimation. The evaluation shows that our new design outperforms that in [28] by up to 31.6% and 30.5% in terms of localization accuracy in the absence and presence of trajectory deviations. Our results improve the understanding of the location and orientation information that can be harnessed from powerline AMF.

Indoor SLAM has been studied extensively. First, we discuss the existing indoor SLAM solutions according to their used sensing modalities. Radar SLAM [30] and lidar SLAM [11] are based on the point clouds generated by radar and lidar. Visual SLAM [29] uses the camera to capture images for landmark detection and map construction. However, the sensing based on radar, lidar, and camera is susceptible to blockages. The limitations of GMF SLAM [53] and Wi-Fi RSS SLAM [1, 13] have been discussed earlier. While Wi-Fi CSI has not been widely applied to SLAM due to its heavy computation burden, in indoor localization tasks, decimeter-level localization accuracy can be achieved with Wi-Fi CSI from the multiple-input multiple-output (MIMO) Wi-Fi devices. Chronos [50] first achieves the decimeter-level localization accuracy with CSI obtained from multiple frequency channels. As the localization accuracy depends on the number of channels monitored by the access point, this approach suffers from large localization delays and localization accuracy drops when the indoor environment lacks enough free channels. EasiTrack [54] uses a MIMO Wi-Fi device and an inertial measurement unit (IMU) to collect multipath CSI and orientation data. However, the CSI phase information is not always available, limiting the application scope of EasiTrack. More recent works use deep learning to learn from labeled Wi-Fi CSI data for indoor navigation and target tracking. In [2], the proposed indoor navigation approach builds the CSI heatmap to localize the target with sub-meter accuracy. However, it requires laborious efforts for map building. The work in [10] uses Wi-Fi CSI data from various positions and during motions to train a machine learning model for localization and target tracking in 3D indoor space. However, the model needs to be retrained when the environment or motions are changed.

Acoustic SLAM [12] constructs a map based on the angles of arrival (AoAs) from multiple infrastructural sound sources. However, the required infrastructure incurs deployment overhead. Differently, the AMFs exploited in this paper are existing infrastructures of indoor spaces. Several SLAM solutions employ GP. The work [44] uses GP as a regressor to derive the continuous occupancy grid map. The work [42] presents a lidar SLAM system that employs a GP map reconstruction method to provide real-time low-drift state estimation and mapping for a robot. The work [22] proposes a method to build a GMF GP by SLAM. The work [13] solves the Wi-Fi SLAM problem using the GP latent variable model to determine the latent-space locations of unlabeled signal strength data. Different from the above studies [13, 22, 42, 44] that integrate GP into the real-time SLAM implemented with filters, this paper integrates GP into GraphSLAM and solves it offline with all odometry and AMF measurement traces for a more accurate and efficient SLAM system. Specifically, the offline processing allows for global optimization to generate a consistent map of the environment, which avoids the local minima situations faced by

the online methods. Besides, solving the SLAM problem offline greatly reduces time and memory complexities as it reduces the real-time map storage and data processing overheads. This can be particularly advantageous when dealing with long trajectories and complex environments. Another new design in this paper is using GP to generate an augmented map covering the nearby regions of the mobile's trajectory to accommodate trajectory deviations during the localization phase. This improves the localization robustness and enables more challenging localization scenarios of the partially in-trajectory and out-trajectory localization. On the contrary, the SLAM studies reviewed above only construct the map along the trajectory of the mobile and perform localization within the map area. This leads to performance degradation, especially in highly variable fields (e.g. AMF).

SLAM has been studied in 3D space, where the SLAM system estimates trajectories in the reconstructed 3D environment. For indoor applications, the authors of [51] use the extended Kalman filter to formulate a 3D GMF-based SLAM aiming to efficiently compensate for drift from odometry measurements. The work [46] introduces a multi-stage 3D SLAM system to localize IoT devices in a 3D indoor space based on Wi-Fi RSS. Except for applications in general indoor spaces, 3D SLAM has also been studied for complex and human-inaccessible environments. The studies in [35, 36] focus on the drilling machine in underground mines and introduce a pose graph SLAM system using re-measurement of the GMF data sequences to predict the pose of the drilling machine. The AMF-based SLAM can be applied in both normal and harsh environments for 3D mapping and localization tasks without the limitations of low discernibility in GMF and unreliability in Wi-Fi RSS.

### 3 TRIAXIAL AMF SENSOR DESIGN AND MEASUREMENT STUDY

In this section, we present the preliminary on AMF. Then, we present the design of the triaxial AMF sensor. Lastly, we present a measurement study to understand AMF's properties.

#### 3.1 Preliminary on Powerline-Induced AMF

A utility powerline has two emanations, i.e., alternating electric and magnetic fields, which are induced by the powerline's ac voltage and current, respectively. In indoor environments, the electric field can be easily shielded or weakened by common materials, while the magnetic field can pass through most materials [32]. In addition, the electric field from the powerline can be easily perturbed by other low-frequency electric fields such as those caused by changes in charge carried by human bodies due to the triboelectric effect and capacitance variations [8, 15]. Thus, this paper focuses on powerline-induced AMF. The AMFs induced by all sources can be superimposed by the following vector addition to form a composite AMF that fills the entire indoor space. Note that the electromagnetic propagation described by Maxwell's theory is irrelevant in the current context, as the alternating electric field induced by the AMF is extremely far away due to the long wavelength of the propagation.

Powerline-induced AMF is from an existing electrical infrastructure, which is abundant indoors but often absent or sparse outdoors. Outdoor overhead or underground powerlines are typically situated at large distances from the user, resulting in diminishing AMF signals. Therefore, in this paper, we only consider indoor environments.

#### 3.2 Design of Triaxial AMF Sensor

**3.2.1 Hardware design and signal pre-processing.** The mechanisms for measuring the low-frequency AMF and the static magnetic field (e.g., GMF) are different. The latter can be measured via magnetism-driven mechanics, which is the basis of the microelectromechanical system (MEMS) design of smartphones' built-in GMF sensors. In contrast, low-frequency AMF needs to be measured via the electromagnetic induction effect. However, as discussed in §1, the inductively excited measurement circuit also creates a secondary AMF. Thus, a triaxial AMF sensor of three independent measurement circuits needs to be carefully designed to avoid cross-axis interference. There are off-the-shelf hand-held AMF meters [39] that are designed for detecting electromagnetic hot spots to

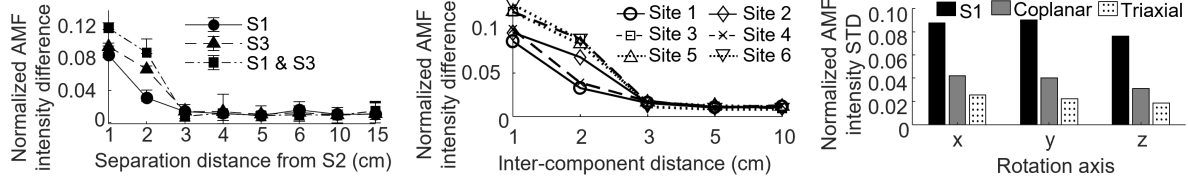


Fig. 4. Impact of inter-component distance on measurement of sensor component  $S_2$ .

Fig. 5. Impact of the inter-component distance on the triaxial arrangement at six sites.

Fig. 6. STD of AMF intensity measured by each setup rotated around a certain axis of  $S_1$ .

avoid unhealthy electromagnetic exposures. These meters are not designed to be highly frequency-selective – they only provide the maximum value within a wide frequency range (e.g., 30 to 300 Hz [39]).

Our triaxial AMF sensor consists of three mutually perpendicular uniaxial AMF sensor components, where each is designed to detect the mains frequency in our region at 50 Hz. The sensor outputs are first sampled by the analog-to-digital converter (ADC) of an STM32 microcontroller at a rate of 1 kilo samples per second (ksps) and then transferred to a Raspberry Pi (Rpi) single-board computer for storage and analysis. From the measurements of a power monitor, the standby and operating powers of the triaxial AMF sensor are 1.06 W and 1.13 W, respectively, which are similar to the powers of Wi-Fi and ultra-wideband (UWB) radios [3].

Fig. 2b shows the configuration of the proposed triaxial sensor formed by three uniaxial sensor components. The three sensor components (denoted by  $S_1$ ,  $S_2$ , and  $S_3$ ) are separated by certain distances, while the centers of their inductor coils are kept colinear. Specifically, as illustrated in Fig. 3b, the separation distances between  $S_1$  and  $S_2$  (denoted by  $d_s$ ) and between  $S_2$  and  $S_3$  (denoted by  $d_{s'}$ ) are determined by a set of experiments shortly to avoid the mutual interference among them. The triaxial sensor applies the following software-based signal pre-processing pipeline. First, it applies a filter with the passband of [49 Hz, 51 Hz] to each sensor component's sampled signal. Then, it computes the root mean square of each sensor component's filtered signal as the signal intensity. Let  $z_{s1}$ ,  $z_{s2}$ , and  $z_{s3}$  denote the signal intensities of the three uniaxial sensor components. The AMF intensity, denoted by  $z$ , is computed as  $z = \frac{1}{z_{\text{ref}}} \sqrt{z_{s1}^2 + (\eta_2 z_{s2})^2 + (\eta_3 z_{s3})^2}$ , where  $\eta_2$  and  $\eta_3$  are two calibration coefficients,  $z_{\text{ref}}$  is a normalization reference. The triaxial sensor returns  $(z_{s1}, z_{s2}, z_{s3}, z)$  when queried. The reading  $z$  is used to construct the 3D AMF intensity map and perform 3D localization; the triaxial readings  $z_{s1}$ ,  $z_{s2}$ ,  $z_{s3}$  are used for orientation sensing. To deal with the hardware fabrication deviations, before the three sensor components are integrated, we use  $S_1$  as the reference to determine  $\eta_2$  and  $\eta_3$ . Specifically, we place each of them sequentially at the same location to collect a data trace. With the three data traces, we determine  $\eta_2$  and  $\eta_3$  such that  $z_{s1} = \eta_2 z_{s2} = \eta_3 z_{s3}$ . To determine  $z_{\text{ref}}$ , we place the triaxial sensor close to a heavy-load electric appliance and use the measurement  $\sqrt{z_{s1}^2 + (\eta_2 z_{s2})^2 + (\eta_3 z_{s3})^2}$  as  $z_{\text{ref}}$ .

**3.2.2 Sensor component separation.** We conduct a set of experiments to determine  $d_s$  and  $d_{s'}$ . First, we fix  $S_2$  at a certain location and record its calibrated reading (i.e.,  $\eta_2 z_{s2}$ ) while  $S_1$  and  $S_3$  are off as the baseline. Denote this baseline reading as  $b_2$ . Then, we switch on  $S_1$  and adjust its location to vary  $d_s$ . During this process, we monitor  $|\eta_2 z_{s2} - b_2|$ , which is referred to as the *intensity difference*. The curve labeled “S1” in Fig. 4 shows the intensity difference versus  $d_s$ , where the error bar represents the mean, minimum, and maximum over 10 measurements. The intensity difference decreases with  $d_s$  when  $d_s$  is from 1 cm to 3 cm. When  $d_s \geq 3$  cm, the intensity difference becomes flatten and minimized. The non-zero intensity difference suggests the mutual interference between  $S_1$  and  $S_2$ . This is because the ac currents in the resonating antenna and the AFE of a uniaxial AMF sensor component also induce a secondary AMF that interferes with the ambient AMF. However, as this secondary AMF

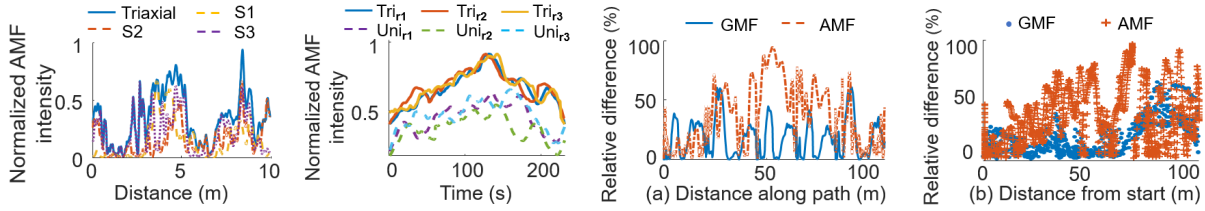


Fig. 7. Normalized AMF in- Fig. 8. Normalized AMF in- Fig. 9. AMF's and GMF's relative difference traces versus (a) tensity trace of sensor com- tensity traces in 3 orienta- the moving distance and (b) the Euclidean distance from the ponents. tions. starting point along a certain path in a lab space.

generated from the low-power sensor is rather weak, its impact on the ambient AMF attenuates quickly with the distance from the sensor. We conduct a similar experiment in which we turn on  $S_3$  and monitor the intensity difference measured by  $S_2$  when  $d_{s'}$  varies. The result is shown by the curve labeled “S3” in Fig. 4. Similarly, when  $d_{s'} \geq 3$  cm, the intensity difference becomes flatten and minimized. In the last experiment, we turn on both  $S_1$  and  $S_3$  and adjust  $d_s$  and  $d_{s'}$  while keeping  $d_s = d_{s'}$ . The intensity difference measured by  $S_2$  is shown by the curve labeled “S1 & S3” in Fig. 4. The curve is higher than those with only  $S_1$  or  $S_3$  turned on, but not simply the sum of the two curves, due to the cross-component inference. From the above results, we set  $d_s = d_{s'} = 3$  cm to minimize the components' mutual inference.

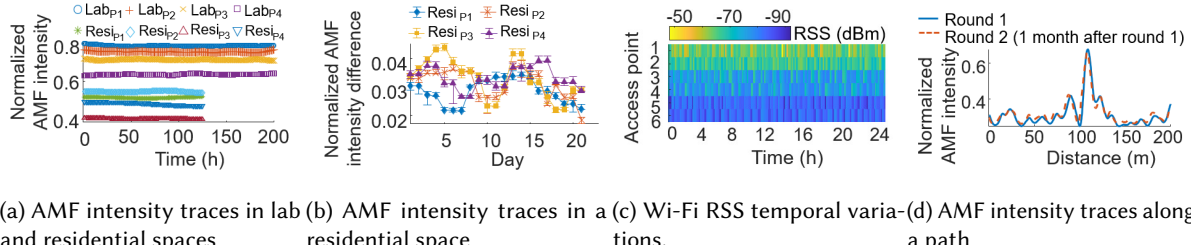
We conduct the above experiment in six indoor environments to investigate whether  $d_s = d_{s'} = 3$  cm is a generalizable good setting. Fig. 5 shows the intensity difference versus  $d_s$ , where we keep  $d_{s'} = d_s$ . In all environments, the intensity difference becomes flatten and minimized when  $d_s$  and  $d_{s'}$  are greater than 3 cm. This suggests that the setting of  $d_s = d_{s'} = 3$  cm is good across various environments.

**3.2.3 Effectiveness of triaxial design.** We conduct experiments to compare our triaxial design with the uniaxial sensor  $S_1$  and an alternative three-sensor design. As illustrated in Fig. 3a, in the alternative coplanar arrangement, the three sensor components have the same orientation and identical separation distances of 5 cm to minimize mutual inference. The comparison among the single uniaxial sensor and the three-sensor arrangements in Fig. 3a and Fig. 3b help understand the contributions from the sensor number and orientation arrangement to the sensing robustness. During the experiments, for each setup, we fix the position of  $S_1$  and rotate the sensor setup clockwise around a certain axis of  $S_1$  with a step size of 30°. We use the standard deviation (STD) of the sensor setup's measurements during the whole rotation process to characterize the robustness of the sensor's AMF measurement to sensor orientation. Fig. 6 shows the STDs of the three setups rotated around the  $S_1$ 's three axes. The uniaxial sensor setup and our proposed triaxial setup yield the highest and lowest STD, respectively. The setup adopting coplanar arrangement yields lower STD compared with the uniaxial sensor setup, as integrating three sensors' measurements can reduce the impact of random measurement noises [49]. However, it is inferior to our proposed triaxial setup that better addresses the vector field nature of AMF.

### 3.3 Measurement Study

We conduct extensive measurements to investigate the spatial, temporal, and orientation properties of AMF using the triaxial AMF sensor. Sensor movements are implemented by a mobile platform with details described in §5.

**3.3.1 Spatial variability.** We collect AMF intensity data along a certain path in the horizontal plane of a lab space hosting normal office appliances such as lights, air conditioners, computers, and printers. Fig. 7 shows the normalized AMF intensity traces of the triaxial sensor and its three sensor components versus the movement



(a) AMF intensity traces in lab and residential spaces (b) AMF intensity traces in a residential space (c) Wi-Fi RSS temporal variations. (d) AMF intensity traces along a path

Fig. 10. Temporal volatility of AMF and Wi-Fi RSS in lab and residential spaces. CV values in (a) are below 0.05. CV values of the normalized Wi-Fi RSS at six access points in (c) are from 0.3323 to 0.5496.

distance along the path. The variations of the AMF intensity with the movement distance suggest the horizontal variability of AMF. In addition, the vector field nature of AMF can be clearly seen, because the measured AMF traces of the three sensor components are different from each other. We also investigate the vertical variability of AMF. Specifically, we move a triaxial AMF sensor and a uniaxial AMF sensor vertically for three rounds, respectively. In the first round, the sensor is kept horizontal. In the following two rounds, the sensor is rotated by 90° clockwise and counterclockwise, respectively. The measured AMF intensity traces are shown in Fig. 8. For both the triaxial and uniaxial sensors (labeled by “Tri” and “Uni” with subscript representing round index), the AMF intensity changes with altitude. Compared with the uniaxial sensor’s traces in the three rounds, the triaxial sensor’s traces are closer to each other. This echoes Fig. 6, where the triaxial sensor is more robust than the uniaxial sensor to orientation variations.

Then, we compare the spatial variabilities of AMF measured by our triaxial sensor and GMF measured by a smartphone. We record the AMF and GMF intensity traces simultaneously along a specific path in the lab space. We compute the *relative difference* of any measured intensity  $z$  with respect to the intensity at the starting point (denoted by  $z_0$ ) as  $\frac{|z-z_0|}{z_0} \times 100\%$ . Fig. 9a shows the relative difference traces versus the moving distance along the path. Fig. 9b visualizes the same data with the Euclidean distance from the starting point as the  $x$  axis. AMF’s relative differences are in general larger than that of GMF. We also compute the *coefficient of variation* (CV) of the collected intensity data, which is the ratio of standard deviation and average value. AMF’s and GMF’s CVs are 0.5013 and 0.2033. Thus, AMF’s spatial variability is more than twice of GMF’s spatial variability.

**3.3.2 Temporal volatility.** We investigate the temporal volatility of AMF under various environments and time scales. We deploy four triaxial AMF sensors at different fixed locations to continuously collect AMF intensity traces over 200 hours. The results are shown by the curves labeled with “Lab” in Fig. 10a. The measured AMF intensity traces are stable over the entire measurement period. The CV values at the four sites are 0.0380, 0.0428, 0.0267, and 0.0390, respectively. We also measure the AMF intensity traces at four fixed locations in a residential space over 120 hours. The results are shown by the curves labeled with “Resi” in Fig. 10a. The traces are also stable. From Fig. 10a, the AMF intensities in the residential space are lower than those in the lab space. This is because the powerlines in the lab space are denser. As residential spaces in general have different occupancy and power usage status during the day time and night time, we particularly compare the AMF intensities measured during day time (7am to 7pm) and night time (7pm to 7am). Specifically, a triaxial AMF sensor collects an intensity reading every hour and computes the difference between a day-time measurement and its corresponding night-time measurement taken 12 hours later. Fig. 10b shows this difference trace over three weeks, where an error bar shows the average, maximum, and minimum values of the day-night difference in a day. The day-night differences are very small, compared with the AMF intensities of about 0.5 as shown in Fig. 10a. This suggests that AMF is temporally stable. As a baseline, we measure the temporal variability of Wi-Fi RSS using a smartphone in the lab

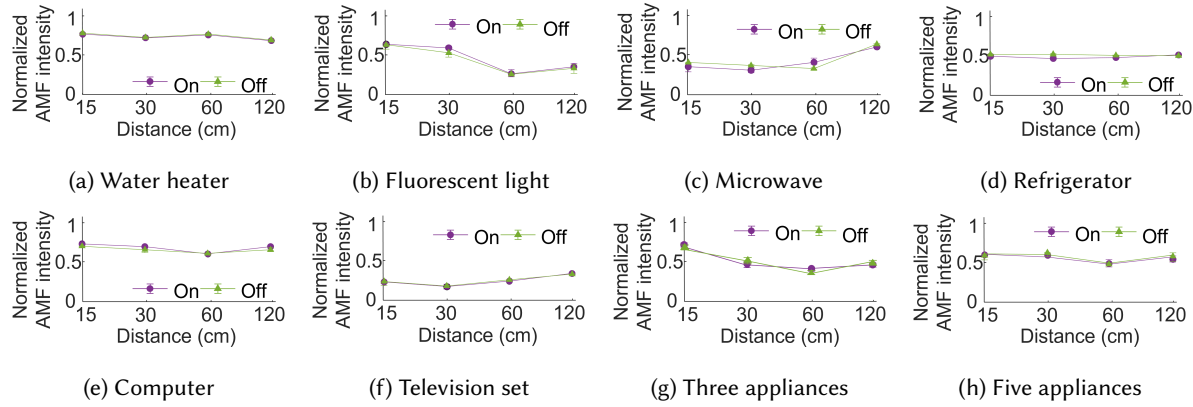


Fig. 11. Impact of electric appliances on AMF intensities measured at various distances from the appliances.

space over 24 hours. Fig. 10c shows the results. To compare the CV values with normalized AMF, we normalize the Wi-Fi RSS data  $w$  using the maximum collected value of  $w_m$  as  $w_n = w/w_m$ . Then, the CVs of the normalized Wi-Fi RSS  $w_n$  are from 0.3323 to 0.5496, which are 7x to 20x higher than the normalized AMF.

We also jointly investigate the spatial variability and temporal volatility. We record the AMF intensity trace when the sensor moves along a path at two times separated by one month. Fig. 10d shows the two AMF intensity traces, which are close. This shows that AMF intensity's spatial distribution is stable over time, which is desirable for SLAM.

Since ac currents in powerlines can change with the operating statuses of electric appliances, we conduct a set of experiments to investigate the impact of the on/off operating statuses of one or more electric appliances on the AMF intensity measurement when the sensor is at various distances from the appliance(s). The appliances include a water heater, fluorescent light, microwave, refrigerator, computer, and television set. The results are shown in Fig. 11. Specifically, from Fig. 11a to Fig. 11f, we can see that the operating statuses of a single appliance generates little impact on the AMF measurements when the sensor-appliance distance is down to 15 cm. This observation is still valid in Fig. 11g and Fig. 11h where we place multiple appliances together and switch them on/off simultaneously. The reason for the above results is that the sensor measurement is dominated by the superposition of the AMFs from all powerlines in the building. This also explains the good temporal stability over many days as presented earlier.

**3.3.3 Effectiveness of GP modeling.** We conduct an experiment to show that GP-based spatial interpolation for AMF outperforms other interpolation methods. To our best knowledge, this is the first in-depth analysis of the effectiveness of GP for modeling powerline-induced 3D AMF with real data.

The prior distribution of a GP is characterized by a mean function  $m(\mathbf{x}) \in \mathbb{R}$  and a covariance function  $k(\mathbf{x}_i, \mathbf{x}_j) \in \mathbb{R}$ , where  $\mathbf{x} \in \mathbb{R}^3$ ,  $\mathbf{x}_i \in \mathbb{R}^3$ , and  $\mathbf{x}_j \in \mathbb{R}^3$  represent locations. The  $m(\mathbf{x})$  represents the prior mean of the AMF intensity at  $\mathbf{x}$ ; the  $k(\mathbf{x}_i, \mathbf{x}_j)$  represents the covariance between the AMF intensities at  $\mathbf{x}_i$  and  $\mathbf{x}_j$ . Due to the lack of prior knowledge about AMF distribution, we adopt  $m(\mathbf{x}) = 0$ . We adopt a covariance function employed for ambient magnetic fields [44]:  $k(\mathbf{x}_i, \mathbf{x}_j) = \sigma_k^2 \cdot \exp\left(\frac{-1}{2 \cdot l_k^2} \|\mathbf{x}_i - \mathbf{x}_j\|_2^2\right)$ , where  $\sigma_k^2$  is the *prior variance* and  $l_k$  is the *length scale*. The  $\sigma_k^2$  and  $l_k$  jointly determine correlation strength. From the above model, the AMF intensity measurements at a set of  $n$  locations  $\{\mathbf{x}_1, \mathbf{x}_2, \dots, \mathbf{x}_n\}$ , denoted by  $\mathbf{z} = \{z_1, z_2, \dots, z_n\}$ , follow the multivariate normal distribution:  $\mathbf{z} \sim \mathcal{N}(\mathbf{0}, \mathbf{K} + \sigma_m^2 \mathbf{I})$ , where  $\mathbf{I} \in \mathbb{R}^{n \times n}$  is the identity matrix, the  $(i, j)^{\text{th}}$  element of the matrix

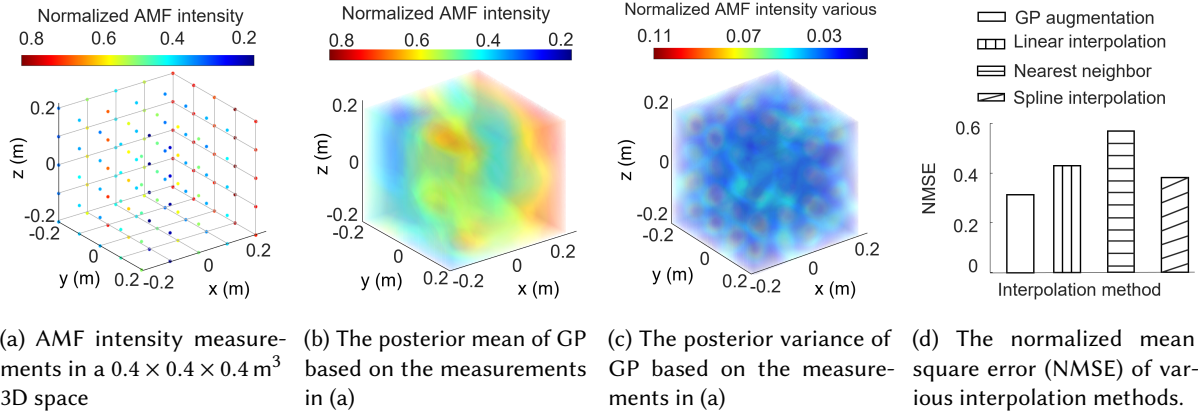


Fig. 12. Visualization of GP-based spatial interpolation; NMSE achieved by various interpolation methods to fit AMF.

$\mathbf{K} \in \mathbb{R}^{n \times n}$  is given by  $K_{i,j} = k(\mathbf{x}_i, \mathbf{x}_j)$ , and  $\sigma_m^2$  is the variance of the AMF sensor's measurement noise. After obtaining an observation of  $\mathbf{z}$  (denoted by  $\tilde{\mathbf{z}}$ ), from the Bayes theorem, for any arbitrary location  $\mathbf{x}$ , the AMF intensity at  $\mathbf{x}$  (denoted by  $z_{\mathbf{x}}$ ) follows the posterior distribution of  $z_{\mathbf{x}} \sim \mathcal{N}(\mu_{\mathbf{x}}, \sigma_{\mathbf{x}}^2)$ , where

$$\mu_{\mathbf{x}} = \mathbf{k}^\top (\mathbf{K} + \sigma_m^2 \mathbf{I})^{-1} \tilde{\mathbf{Z}}, \quad \sigma_{\mathbf{x}}^2 = \sigma_k^2 - \mathbf{k}^\top (\mathbf{K} + \sigma_m^2 \mathbf{I})^{-1} \mathbf{k}, \quad (1)$$

and  $\mathbf{k} = [k(\mathbf{x}, \mathbf{x}_1), k(\mathbf{x}, \mathbf{x}_2), \dots, k(\mathbf{x}, \mathbf{x}_n)]^\top$ . In other words, with  $\tilde{\mathbf{z}}$ , we can predict the AMF intensity at  $\mathbf{x}$  as  $\mu_{\mathbf{x}}$  with an uncertainty level characterized by  $\sigma_{\mathbf{x}}^2$ . Therefore, with AMF intensity measurements at finite locations, the measurements and the posterior distributions at all locations form a *GP-augmented AMF*. The GP model requires three hyperparameters  $\sigma_k$ ,  $l_k$ , and  $\sigma_m$ , which can be estimated by the maximum likelihood estimation approach with training data [16].

We conduct measurements to visualize the GP-augmented AMF. The 6DoF robotic arm carries a triaxial AMF sensor to take measurements in a  $0.4 \times 0.4 \times 0.4$  m $^3$  cubic space. As the robotic arm control software provides the arm's real-time location, we can obtain the location of the AMF sensor during the process. Prior to this experiment, we estimate  $\sigma_m^2$  using data collected at a fixed location. Fig. 12a shows the AMF intensity measurements collected at 125 locations. We estimate the hyperparameters  $\sigma_k$  and  $l_k$  using the measurements and the associated locations. Then, we apply Eq. (1) to generate a GP-augmented AMF at dense locations in the cubic space. Figs. 12b and 12c show the GP's posterior mean and variance. The GP's posterior mean provides a smooth and quasi-continuous estimation of the AMF intensity.

We compare the GP augmentation with several other interpolation methods, i.e., nearest neighbor, linear, and spline. We reserve the measurements at 20 locations randomly selected from the 125 locations shown in Fig. 12a as the testing data. Then, we feed the measurements at the remaining 105 locations to the various interpolation methods to predict the measurements at the 20 locations. Fig. 12d shows the normalized mean square error (NMSE) of the predicted values using each interpolation method. NMSE is the ratio of the mean square error and the mean of the true values. GP augmentation achieves the lowest NMSE. This suggests that GP characterizes the AMF more effectively.

**3.3.4 Angular stability of AMF.** We assume that the angle of the AMF vector at a certain location is fixed, which is the basis for estimating the orientation variation when the triaxial AMF sensor re-visits the location. We conduct measurements to verify the assumption. Denote by  $(z_{s1}, z_{s2}, z_{s3})$  and  $(z'_{s1}, z'_{s2}, z'_{s3})$  the readings of the triaxial AMF sensor when it is at a certain position but oriented to two different directions. Denote by

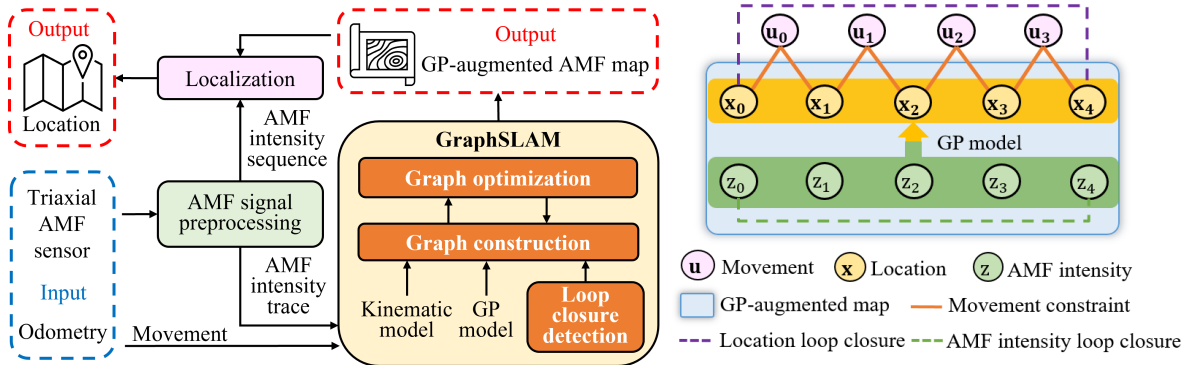


Fig. 13. Approach overview.

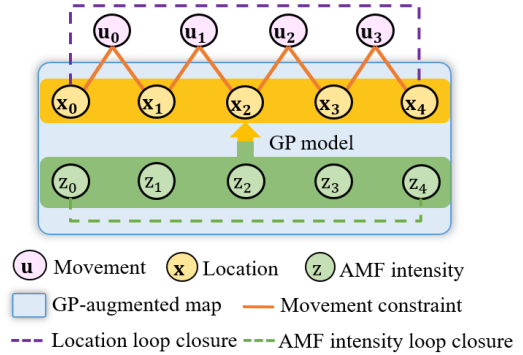


Fig. 14. GraphSLAM representation.

$(\alpha, \beta, \gamma)$  the angular difference between the local coordinate systems of the sensor in the two orientations. Specifically, the second coordinate system is obtained by rotating the first coordinate system around its third, second, and first axes sequentially for  $\alpha$ ,  $\beta$ , and  $\gamma$  degrees. If the assumption holds, we have  $[z_{s1}, \eta_2 z_{s2}, \eta_3 z_{s3}]^\top = R(\alpha, \beta, \gamma)[z'_{s1}, \eta_2 z'_{s2}, \eta_3 z'_{s3}]^\top$ , where the detailed expression of the rotation matrix  $R(\alpha, \beta, \gamma) \in \mathbb{R}^{3 \times 3}$  can be found in [18]. In our measurements, we fix the location of the triaxial AMF sensor and rotate it along each axis by different angles for multiple times. Then, we calculate the AMF intensity for each rotation. The AMF intensity remains almost constant with a standard deviation of 0.0117 over nine orientations. This suggests that the AMF vector has rotational invariance [7, 31] and conforms to the rotation matrix relationship. We also examine the stability of the measurement trace in each axis when the sensor is placed at a fixed location with a fixed orientation over a long time. For the trace labeled “Resip<sub>P1</sub>” in Fig. 10a, the standard deviations in the three axes are 0.0255, 0.0302 and 0.0197. This suggests that the angle of the AMF vector at a certain location is stable over time.

#### 4 GP-ASSISTED SLAM IN AMF

This section designs the GP-assisted orientation-aware 3D SLAM in 3D AMF. §4.1 overviews the approach. §4.2 and §4.3 present GraphSLAM, localization and orientation sensing.

##### 4.1 Approach Overview for Location SLAM

Fig. 13 shows the algorithm blocks of the approach. We assume that the mobile has triaxial AMF sensing and odometry capabilities. We do not assume a specific odometry mechanism. For instance, on a wheel-based robot, odometry can be achieved by monitoring the wheel rotation and steering; on a flying drone, odometry can be achieved by dead reckoning with accelerometer and gyroscope data. Most odometry mechanisms are subject to the problem of error accumulation over long run [4]. Thus, odometry alone is insufficient for the accurate reconstruction of long-run movement trajectory. The mobile continuously collects the AMF data, applies the pipeline of signal pre-processing presented in §3.2 to produce the AMF intensity trace, and segments the trace into sequences with the length identical to the sampling interval of the odometry. In what follows, we present an overview of the two main components of the proposed approach, i.e., GraphSLAM and localization.

We adopt GraphSLAM, a widely used technique in robotics, to reconstruct the mobile’s trajectory and generate a GP-augmented AMF map. GraphSLAM can be formulated as a non-linear least squares problem. The GraphSLAM component consists of the following three algorithm modules. (1) The *loop closure detection* module identifies the revisited locations in terms of AMF intensity. The detected loop closures provide important information to rectify the long-run drifts of odometry. (2) The *graph construction* module uses the kinematic model on the odometry

data, the GP model on the AMF intensity data, as well as the loop closures to build the graph structure. (3) The *graph optimization* module finds the optimal graph by minimizing the regularization cost jointly defined from the kinematic model, GP model, and the identified loop closures. Then, the movement trajectory can be derived from the optimal graph. Lastly, the GP-augmented AMF map is formed by tagging AMF intensity data onto the reconstructed trajectory and updating the GP posteriors for the locations not visited.

After the GP-augmented AMF map is constructed, a mobile can be localized by matching the captured odometry and AMF intensity sequences with the map. Note that we use the AMF intensity sequence during movement rather than a single AMF intensity sample for localization. This is because that multiple locations in the map may have similar AMF intensity values that cause ambiguity. Using a sequence for matching largely reduces the chance of ambiguity. The matching minimizes the regularization cost jointly defined from the kinematic model and the posteriors in the GP-augmented AMF map.

## 4.2 GP-Assisted GraphSLAM

In this section, we use  $t \in \mathbb{Z}$  to denote the discrete time step index. Suppose there are a total of  $n$  time steps for SLAM, i.e.,  $t \in [1, n]$ . In what follows, we describe the details of the three algorithm modules.

**4.2.1 Loop closure detection.** Loop closure detection determines whether a given location is revisited by the mobile based on AMF intensity. A *loop closure pair*  $(i, j)$  contains two time step indexes  $i \in [1, n]$  and  $j \in [1, n]$  ( $i < j$ ), at which the mobile visits the same location. Denote by  $C$  the set of all detected loop closure pairs.

Our loop closure detection is based on an AMF intensity sequence consisting of multiple consecutive AMF intensity measurements instead of a single AMF intensity measurement, to reduce the false positives caused by the aforementioned ambiguity problem. Specifically, at each time step  $t$ , the AMF intensity measurement sequence of length  $l$  obtained in the time duration  $[t - l + 1, t]$  is matched against a sliding window of length  $l$  in the historical trace over the time duration  $[1, t - 1]$  in terms of Euclidean distance. When the Euclidean distance is smaller than a threshold  $\tau$ , the two corresponding sequences are marked as loop closure candidates. We apply the following further checks on the loop closure candidates, aiming at eliminating all false positives. First, by checking the timestamps, the candidate pairs with short time spans between the pair members are excluded to avoid creating too brief loops that tend to be false positives. Then, for all candidate pairs involving the same location (e.g.,  $\{(i, j_1), (i, j_2), (i, j_3)\}$ ), the remaining locations (i.e.,  $j_1, j_2$ , and  $j_3$  in the above example) should have AMF intensity sequences similar to each other. Thus, we check the Euclidean distances among the remaining locations' AMF intensity sequences and pass the candidate pairs only when the Euclidean distances are all smaller than a threshold  $\tau$ . In §5.2, we determine the setting of  $\tau$  via experiments.

**4.2.2 Graph construction.** As illustrated in Fig. 14, the GraphSLAM formulation can be represented by a graph of relationships between states (i.e., locations) and observations (i.e., odometry and AMF measurements). The objective of GraphSLAM is to estimate the trajectory  $X = \{\mathbf{x}_t | t \in [1, n]\}$  based on the observation trace  $\{z_t, \mathbf{u}_t | t \in [1, n]\}$  to minimize the regularization costs arising from the odometry and AMF sensing that are represented by the edges in the graph. The regularization is derived from the kinematic, loop closure, and GP models. The are described as follows.

*Kinematic model regularization.* The odometry measurement  $\mathbf{u}_t$  that connects  $\mathbf{x}_{t-1}$  and  $\mathbf{x}_t$  records the relative displacement in position and orientation of the mobile from time  $t - 1$  to  $t$ . This state transition is governed by the kinematic model of the odometry, which can be abstracted as  $\mathbf{x}_t = h_o(\mathbf{x}_{t-1}, \mathbf{u}_t)$ . The detailed closed-form expression of the kinematic model  $h_o(\cdot)$  depends on the specific odometry mechanism. Specific 3D kinematic model examples can be found in [5, 47]. For a time step  $t$ , we use the Euclidean distance  $\|h_o(\mathbf{x}_{t-1}, \mathbf{u}_t) - \mathbf{x}_t\|_{\ell_2}$  to characterize the compliance with the kinematic model. For the whole trajectory, we use the following sum of squares to characterize the overall compliance with the kinematic model:  $\sum_{t=2}^n \|h_o(\mathbf{x}_{t-1}, \mathbf{u}_t) - \mathbf{x}_t\|_{\ell_2}^2$ .

**Algorithm 1** Graph optimization of GP-assisted SLAM

**Input:** Odometry data trace  $\{\mathbf{u}_t | t \in [1, n]\}$ , AMF intensity trace  $\{z_t | t \in [1, n]\}$ , loop closure pairs  $C$

**Output:** Reconstructed trajectory  $X^* = \{\mathbf{x}_1^*, \dots, \mathbf{x}_n^*\}$ , and the GP-augmented map  $\{(\mathbf{x}, \mu_{\mathbf{x}}) | \forall \mathbf{x}\}$

- 1: Compute trajectory  $X_{\text{NoGP}}$  using Eq. (2)
- 2: Determine the search space  $\Omega = \bigcup_{t=1}^n \Omega_t$  in the proximity of  $X_{\text{NoGP}}$  using Eq. (3)
- 3: Compute GP posterior mean  $\mu_{\mathbf{x}}$  for every location  $\mathbf{x} \in \Omega$  using Eq. (1)
- 4: Compute the optimal trajectory  $X^*$  in the searching space  $\Omega$  using Eq. (4)
- 5: Generate the GP-augmented map  $\{(\mathbf{x}, \mu_{\mathbf{x}}) | \forall \mathbf{x}\}$  with the data  $\{(\mathbf{x}_t, z_t) | t \in [1, n]\}$  using Eq. (1)
- 6: Return  $X^*$  and GP-augmented map

*Loop closure regularization.* We use  $k$  consecutive odometry measurements recursively on the kinematic model by  $h_o(\mathbf{x}_{t-1}, \mathbf{u}_t, \mathbf{u}_{t+1}, \dots, \mathbf{u}_{t+k}) = h_o(h_0(\dots, (h_0(\mathbf{x}_{t-1}, \mathbf{u}_t), \mathbf{u}_{t+1}), \dots), \mathbf{u}_{t+k})$ , which gives  $\mathbf{x}_{t+k}$ . With the loop closure detection result  $C$ , i.e., the set of all detected loop closure pairs, we use the following term to characterize the inconsistency between the odometry result and loop closure detection result:  $\sum_{\forall(i,j) \in C} \|h_o(\mathbf{x}_i, \mathbf{u}_{i+1}, \mathbf{u}_{i+2}, \dots, \mathbf{u}_j) - \mathbf{x}_j\|_{\ell_2}^2$ . For the illustration shown in Fig. 14, the locations  $\mathbf{x}_0$  and  $\mathbf{x}_4$  form a loop closure. Thus,  $C = \{(0, 4)\}$ .

*GP model regularization.* Prior to SLAM, the GP hyperparameters (i.e.,  $\sigma_k$ ,  $l_k$ , and  $\sigma_m$ ) are obtained. With all the measured AMF intensities  $\{z_t | t \in [1, n]\}$  at the locations  $\{\mathbf{x}_t | t \in [1, n]\}$ , we use Eq. (1) to compute the posterior distributions of the AMF intensities characterized by the following posterior mean vector and covariance matrix:  $\boldsymbol{\mu}_X = [\mu_{\mathbf{x}_1}, \mu_{\mathbf{x}_2}, \dots, \mu_{\mathbf{x}_n}]^\top$  and  $\Sigma_X = \text{diag}(\sigma_{\mathbf{x}_1}^2, \sigma_{\mathbf{x}_2}^2, \dots, \sigma_{\mathbf{x}_n}^2)$ . For a location  $\mathbf{x}$ , we can use the Euclidean distance  $\|\mu_{\mathbf{x}} - z_{\mathbf{x}}\|_{\ell_2}$  to characterize the compliance with the GP posterior. For the whole trajectory, we can use the following sum of squares to characterize the overall compliance with the GP posteriors:  $\sum_{t=1}^n \|\mu_{\mathbf{x}_t} - z_{\mathbf{x}_t}\|_{\ell_2}^2$ .

**4.2.3 Graph optimization.** By minimizing the sum of the regularization costs from the kinematic, loop closure, and GP models, GraphSLAM obtains a globally consistent estimation of the trajectory. The procedure of the graph optimization is presented in Algorithm 1. It starts from the initialization chaining together the kinematic model and the loop closures. Specifically, we compute a trajectory  $X_{\text{NoGP}}$  using the conventional GraphSLAM problem that does not involve GP:

$$X_{\text{NoGP}} = \arg \min_{X=\{\mathbf{x}_1, \dots, \mathbf{x}_n\}} \sum_{t=2}^n \|h_o(\mathbf{x}_{t-1}, \mathbf{u}_t) - \mathbf{x}_t\|_{\ell_2}^2 + \sum_{\forall(i,j) \in C} \|h_o(\mathbf{x}_i, \mathbf{u}_{i+1}, \mathbf{u}_{i+2}, \dots, \mathbf{u}_j) - \mathbf{x}_j\|_{\ell_2}^2. \quad (2)$$

Based on the trajectory  $X_{\text{NoGP}}$ , we aim to find a further optimized trajectory  $X^*$  that jointly considers the kinematic, loop closure, and GP regularization. To reduce the computation overhead, we limit the search space for  $X^*$  to the proximity of  $X_{\text{NoGP}}$ . The rationale of this limitation is that the GP model has increased uncertainties for the locations far away from the locations with measurements. We illustrate this with real measurements. Specifically, taking a reference point in 3D space, we collect AMF measurements at locations with various distances in the covariance function's length scale  $l_k$  from this reference point. Then, we calculate the relative error between the real measurements and the GP's posterior means at these measured locations. Fig. 15 shows the results. We can see an increasing trend of the relative error. In our graph optimization implementation, we search for the new locations for  $X^*$  within  $1.5l_k$  from the locations in  $X_{\text{NoGP}}$ . The search space is  $\Omega = \bigcup_{t=1}^n \Omega_t$ , where

$$\Omega_t = \{\mathbf{x}'_t | \|\mathbf{x}'_t - \mathbf{x}_t\|_{\ell_2} \leq 1.5l_k, \mathbf{x}_t \in X_{\text{NoGP}}, \forall \mathbf{x}'_t \in \mathbb{R}^3\}. \quad (3)$$

The GP's posterior mean  $\mu_{\mathbf{x}}$  for the location  $\mathbf{x} \in \Omega$  is computed using Eq. (1). Then, by minimizing the overall regularization cost from the kinematic, loop closure, and GP models, the further optimized trajectory  $X^* = \{\mathbf{x}_1^*, \dots, \mathbf{x}_n^*\}$  is computed by:

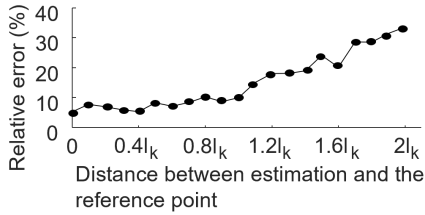


Fig. 15. Relative error of the GP's posterior means at locations with distances in covariance function's length scale  $l_k$  from a measurement point in the AMF.

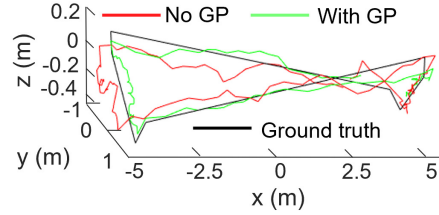


Fig. 16. Reconstructed trajectories without and with the GP regularization. The corresponding mean square errors are 0.37 m and 0.29 m, respectively.

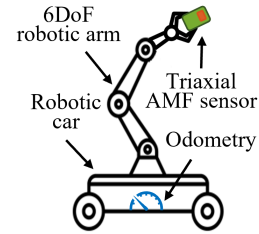


Fig. 17. Mobile platform

$$\mathcal{X}^* = \arg \min_{\substack{\mathcal{X} = \{\mathbf{x}_1, \dots, \mathbf{x}_n\}, \\ \mathbf{x}_t \in \Omega_t, t=1, \dots, n}} \sum_{t=2}^n \|h_o(\mathbf{x}_{t-1}, \mathbf{u}_t) - \mathbf{x}_t\|_{\ell_2}^2 + \sum_{t=1}^n \|\mu_{\mathbf{x}_t} - \mathbf{z}_t\|_{\ell_2}^2 + \sum_{\forall (i,j) \in C} \|h_o(\mathbf{x}_i, \mathbf{u}_{i+1}, \mathbf{u}_{i+2}, \dots, \mathbf{u}_j) - \mathbf{x}_j\|_{\ell_2}^2. \quad (4)$$

Essentially, Eq. (4) is a nonlinear least squares problem, which can be solved iteratively by the Levenberg Marquardt method [40]. Lastly, with the reconstructed map  $\{(\mathbf{x}_t^*, z_i) | t \in [1, n]\}$ , this module computes the GP posteriors for all locations using Eq. (1), forming the GP-augmented map.

Now, we use an example to illustrate the benefit brought by the GP model regularization. We move a triaxial AMF sensor along a trajectory in the 3D space by using the aforementioned mobile platform. The ground-truth trajectory is shown by the black straight line segments in Fig. 16. The red curve is the reconstructed trajectory  $\mathcal{X}_{\text{NoGP}}$  given by Eq. (2), whereas the green curve is the  $\mathcal{X}^*$  given by Eq. (4). The mean square errors (MSEs) of  $\mathcal{X}_{\text{NoGP}}$  and  $\mathcal{X}^*$  from the ground truth are 0.37 m and 0.29 m, respectively. Thus, owing to the GP regularization, the trajectory reconstruction accuracy is improved by about 22%.

### 4.3 Localization and Orientation Sensing

During the localization phase, given a measurement sequence over  $m$  consecutive time steps as  $\{z_t, \mathbf{u}_t | t \in [1, m]\}$  and the GP-augmented map  $\{(\mathbf{x}, \mu_{\mathbf{x}}) | \forall \mathbf{x}\}$ , the movement trajectory  $\hat{\mathcal{X}} = \{\hat{\mathbf{x}}_1, \dots, \hat{\mathbf{x}}_m\}$  can be estimated by solving  $\hat{\mathcal{X}} = \arg \min_{\mathcal{X} = \{\mathbf{x}_1, \dots, \mathbf{x}_m\}} \sum_{t=2}^m \|h_o(\mathbf{x}_{t-1}, \mathbf{u}_t) - \mathbf{x}_t\|_{\ell_2}^2 + \sum_{t=1}^m \|\mu_{\mathbf{x}_t} - \mathbf{z}_t\|_{\ell_2}^2$ .

Given two AMF readings  $(z_{s1}, z_{s2}, z_{s3})$  and  $(z'_{s1}, z'_{s2}, z'_{s3})$  collected at the same location, where the location is determined by GraphSLAM or localization, the AMF sensor rotation angle  $(\alpha, \beta, \gamma)$  can be solved from the rotation equation presented in §3.3 using the technique from [18]. We can use the odometry-based orientation sensing result when the mobile visits the location for the first time as the base orientation and the rotation angles estimated from AMF readings to derive the orientations for all the subsequent re-visits. Our results in §5.2 show that this AMF-based orientation sensing is free of the error accumulation problem faced by odometry.

## 5 PERFORMANCE EVALUATION

We conduct experiments with known ground truth in various environments to evaluate the performance of AMF-based GP-assisted SLAM in the aspects of loop closure detection, map construction, localization, and orientation sensing.

## 5.1 Experiment Setup

**5.1.1 Mobile platform and data collection.** We set up a mobile platform to automate the controlled experiments that can collect AMF/GMF/Wi-Fi and odometry data as well as the ground-truth trajectories in indoor environments. As illustrated by Fig. 17, we mount a 6DoF robotic arm (Interbotix WidowX 250) onto a wheel-based robot (Turtlebot 3 Burger). The robotic arm clamps the triaxial AMF sensor. The robot and arm are controlled by two Raspberry Pi single-board computers separately that run Robot Operating System (ROS). The robot provides the capability of roaming in the target space by following a predefined trajectory on the floor plane; the 6DoF robotic arm provides the capability of alternating altitude and orientation of the AMF sensor. By following coordinated movement scripts specified to the robot and the arm, the AMF sensor's movement forms a known trajectory in the 3D space as the ground truth. The robot's and arm's built-in odometries are sampled at 10 samples per second (sps). These two odometries are combined to form a single odometry based on the known relationship between the robot's and the arm's coordinate systems. The triaxial AMF sensor is sampled at 1 ksp. For comparison, we use the same mobile platform to carry a smartphone (Samsung Galaxy S7) to collect the GMF and Wi-Fi RSS data along the same trajectory at the sampling rate of 100 sps and 0.2 sps, respectively. All data traces are offline analyzed.

**5.1.2 Evaluated indoor sites.** We conduct experiments in eight indoor sites with different powerline distributions and densities of appliances as shown in Fig. 18. At each site, we predetermine the 3D trajectories  $T_M$  and  $T_L$  for mapping and localization, respectively. The ground truth data of these trajectories are obtained by the following procedures. First, we measure the position and orientation of the AMF sensor at the starting point of each trajectory as the initial values. Next, we use kinematic models to calculate the position and orientation of the AMF sensor at every sampling instant of the odometry based on known information from the mobile platform, which are the constant translational velocity of 0.1 m/s and a constant rotational velocity of 0.2 rad/s as well as the movement control commands. Then, by attaching the calculated results orderly after the initial values, we obtain the 3D location trace where the mobile platform would pass by when following the trajectory. In the experiments, we make marks on the ground or draw lane lines as references to check whether the mobile platform correctly executes the control commands and accurately follows the trajectory. This ensures the quality of the ground truth data. During mapping, we command the mobile platform to follow the predefined trajectory  $T_M$  for multiple loops continuously at the constant velocity. Fig. 21a shows the predefined trajectory in Lab A. The collected data trace is used for map construction. During localization, we command the mobile platform to follow the predefined trajectory  $T_L$ . Each short signal sequence collected on  $T_L$  is used to perform localization. To evaluate the robustness against trajectory deviations during the localization phase, we consider three cases: i)  $T_L$  is the same as  $T_M$ , ii)  $T_L$  is close to  $T_M$  and has crossings with  $T_M$ , iii)  $T_L$  has no crossings with  $T_M$ . The results reported in this section are obtained under the first case unless specified otherwise. The enclosed areas, lengths, and altitude variations of the ground-truth trajectories at the eight sites are summarized in Table 1.

Table 1. Statistics of the ground-truth trajectory during mapping phase.

Site	Lab A	Lab B	Office lobby	Demo room	Display room	Print room	Car park	Library
Enclosed area ( $\text{m}^2$ )	8	53.2	58	10.6	32.5	33.5	548.5	421.4
Length (m)	18.6	45.6	63.8	13.3	27.9	26.2	133.2	87.7
Altitude variation (cm)	40	10	30	40	50	40	45	40



Fig. 18. Evaluated indoor environments.

## 5.2 Evaluation Results

**5.2.1 Loop closure detection performance.** In loop closure detection, the similarity metric needs to distinguish between true and false loop closures when comparing the AMF intensity sequences. To find a valid similarity metric, we compare the ambiguity discrimination abilities of typical similarity metrics [48], which are the Euclidean distance, cosine distance and Pearson correlation distance. For each metric, the distances of all possible combinations of two AMF intensity sequences are represented by a similarity matrix, where a smaller element indicates that the two AMF intensity sequences have a bigger chance to be a loop closure pair. Considering a single-loop AMF intensity trace, the similarity matrix of an ideal metric will show small diagonal terms with prominent differences from the large off-diagonal terms. Fig. 19 shows the performance of different similarity metrics based on the same single-loop AMF intensity trace. In Fig. 19a, there is a clear concentration of small values in diagonal positions, which indicates that the Euclidean distance metric can efficiently identify loop closures using a threshold. While in Fig. 19b and Fig. 19c, many off-diagonal terms have similar small values as the diagonal terms, which makes it difficult for the cosine distance and Pearson correlation distance to distinguish loop closures by a threshold. Therefore, we apply the Euclidean distance with a threshold as the criterion for loop closing detection based on AMF intensity sequences.

As discussed in §4.2, the threshold  $\tau$  is an important hyperparameter of the loop closure detection. Its proper setting depends on the AMF. When the AMF contains large spatial deviations, the collected AMF intensity trace has more fluctuations. If the threshold  $\tau$  is too small, more true loop closure pairs will be missed. In contrast, when the AMF intensity field is even, a too large setting for  $\tau$  may lead to excessive false positive loop closure pairs. Empirically, a few false positives can greatly impair the map reconstruction performance, whereas false negatives have a much lower impact on the map reconstruction. Thus, we aim to find a setting for  $\tau$  that maintains low false positive rates in a range of indoor environments. To this end, we measure the receiver operating characteristic (ROC) of the loop closure detection algorithm in four indoor sites. Fig. 20 shows the ROC curves, where each curve is obtained by varying  $\tau$ . The false positive rate (FPR) is measured by the percentage of non-loop closure pairs wrongly detected as loop closure pairs; the true positive rate (TPR) is measured by the percentage of loop

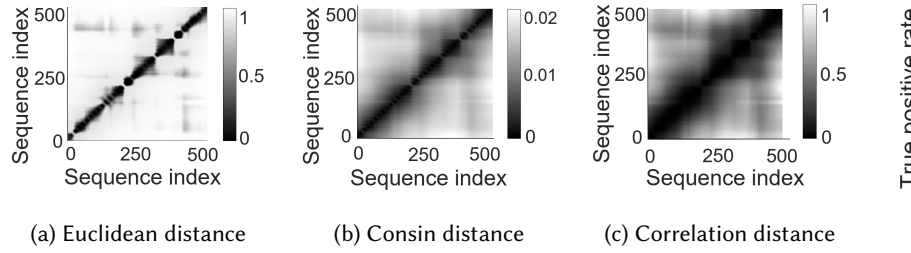


Fig. 19. Comparsion of similarity measures of AMF intensity sequences.

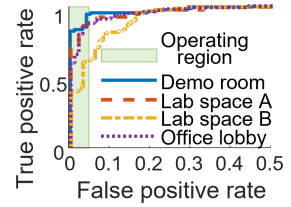


Fig. 20. ROCs of loop closure de-ttection.

closure pairs correctly detected. As the AMF distribution varies for different sites, the ideal settings for  $\tau$  at all sites, which lead to the respective maximum TPR subject to zero FPR, may not be the same. As such, we find the largest universal  $\tau$  setting such that the resulting operating points on the four ROC curves fall within the shaded area shown in Fig. 20 with  $FPR \leq 4\%$ . Empirically, 4% is an acceptable FPR that does not lead to severe impairment of map reconstruction.

**5.2.2 Mapping performance.** We conduct a set of experiments in Lab A by following the designed trajectory shown in Fig. 21a, in which the AMF/smartphone carried by the robotic arm experiences both horizontal and vertical movements in the 3D space.

*Visualization of reconstructed trajectories.* Fig. 21b shows the trajectory reconstructed from the odometry only. The large deviations from the ground truth are due to cumulative errors over long runs. Fig. 21c shows the trajectories reconstructed by SLAM based on the uniaxial and triaxial AMF sensors, respectively. Compared with the result shown in Fig. 21b, both the uniaxial and triaxial AMF sensors improve the reconstruction accuracy because the odometry drift can be rectified by AMF sensing. In addition, visually, the reconstruction by the triaxial AMF sensor is closer to the ground truth. We will present the improvement quantification shortly. Fig. 21d compares the trajectories reconstructed by triaxial AMF data with and without GP regularization. Visually, with GP regularization, the reconstructed trajectory is closer to the ground truth.

*Visualization of constructed maps.* Fig. 22a shows the map constructed by tagging the measured AMF intensities (represented by colors) onto the trajectory reconstructed using Eq. (2) without the GP regularization in the graph optimization and also without GP augmentation. Therefore, the map provides limited information on in-trajectory AMF intensities. Fig. 22 shows the GP-augmented map. Specifically, the trajectory shown by the black curve is reconstructed by Algorithm 1 with the GP regularization in the graph optimization. In addition, the GP posteriors are used to augment the map. Therefore, the augmented map fills up the entire space and can better support localization when the mobile's movement deviates from the map trajectory.

*Mapping performance of various sensing modalities.* Fig. 23a shows the cumulative distribution functions (CDFs) of the individual errors of the trajectories reconstructed by SLAM systems with various sensing modalities in Lab A, where the individual error is the Euclidean distance between a location in the recovered trajectory and the corresponding location in the ground truth trajectory. We use the mean error, i.e., the average value of all individual errors, as a nutshell metric to describe the overall performances of different SLAM systems. The SLAM systems based on Wi-Fi RSS and odometry have large mapping errors. Specifically, the mean mapping error based on Wi-Fi RSS is 1.47 m. The GMF-based SLAM gives a mean error of 0.56 m, which is 17.3% larger than that of the SLAM based on uniaxial AMF sensing, i.e., 0.46 m. Among the AMF-based SLAM systems, the mapping accuracy is improved by upgrading from uniaxial to triaxial sensing and then by integrating GP regularization. The most outperforming SLAM system, i.e., triaxial AMF with GP, achieves a mean error of 0.31 m.

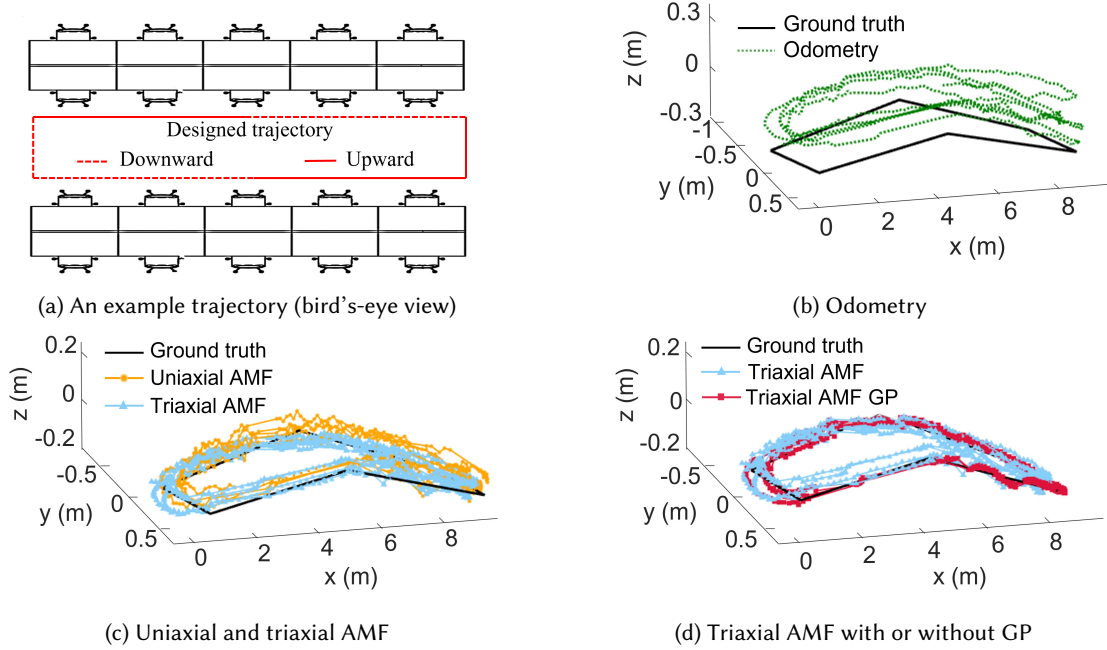


Fig. 21. Reconstructed trajectories with odometry only, uniaxial and triaxial AMF sensors, with and without GP.

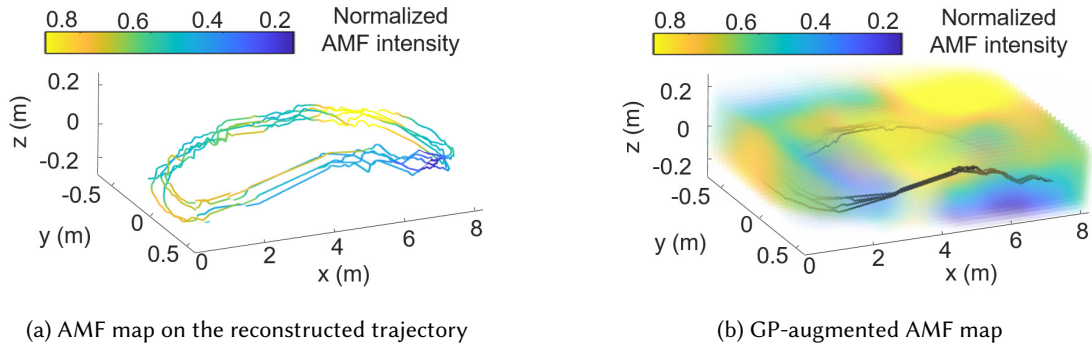


Fig. 22. Constructed AMF maps.

*Mapping performance at eight sites.* We evaluate the mapping performance of the triaxial and uniaxial AMF-based SLAM systems at all eight sites. Fig. 24a shows the box plots of the mapping errors, where a box's central line indicates the median, the bottom and top edges indicate the 25th and 75th percentiles, the whiskers represent the non-outlier extreme values. The mapping achieves sub-1.5m median errors and its performance slightly varies in the first six indoor environments, because the powerline distributions and the electrical loading of these environments are different. In the two larger sites of the car park and library, the mapping has larger median errors but still within 2m, because of the lower density of electrification. The uniaxial and triaxial AMF based systems have comparable median errors in environments with small area and dense powerline distribution such

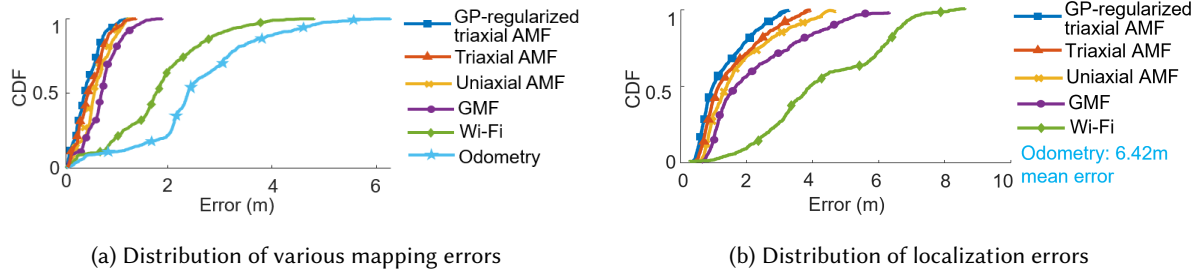


Fig. 23. Mapping and localization performances of various sensing modalities in Lab A.

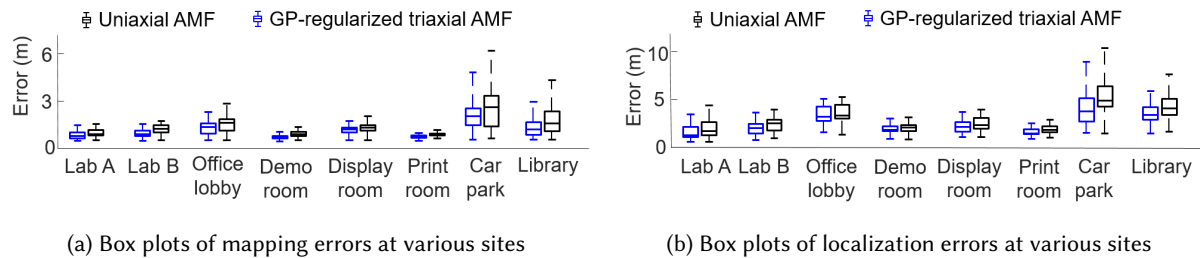


Fig. 24. Performances of mapping and localization conducted within the map trajectory.

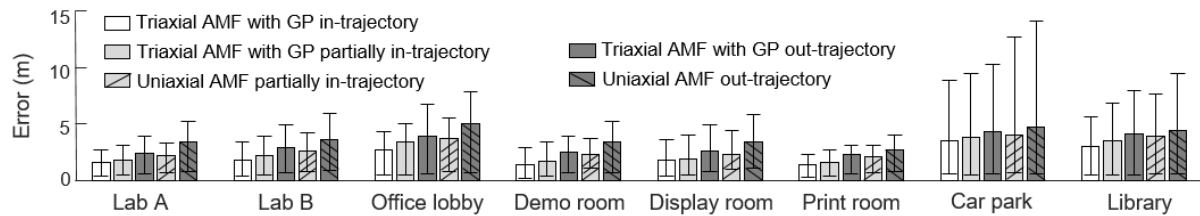


Fig. 25. Performance of in-trajectory, partially in-trajectory, and out-trajectory localization based on (1) triaxial AMF with GP regularization and augmentation and (2) uniaxial AMF without GP regularization and augmentation.

as the demo room and print room. However, the triaxial AMF sensing consistently outperforms the uniaxial AMF sensing at all sites. This superiority is more pronounced when the environment has relatively sparse powerline distribution, e.g., office lobby, or covers a large area, e.g., car park and library. This suggests the better capability of the triaxial AMF sensing in dealing with larger and more challenging environments.

**5.2.3 Localization performance.** The localization performance is closely related to the quality of the map. Different from most existing SLAM studies [13, 19] that only perform localization within the trajectory of the map, the GP-augmented map enables the localization in the nearby region of the trajectory. Thus, we consider three scenarios: (i) *In-trajectory localization*: We use either the map constructed by Eq. (2) without the GP regularization or the map constructed by Eq. (4) with the GP regularization. During the localization phase, the mobile still exactly follows the map trajectory. (ii) *Partially in-trajectory localization*: Based on the GP-augmented map, during the localization phase, the mobile's ground-truth trajectory is close to and has crossings with the map trajectory. (iii)

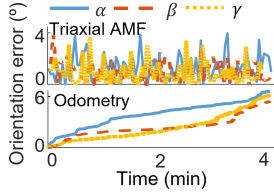


Fig. 26. Triaxial AMF sensor and odometry orientation errors.

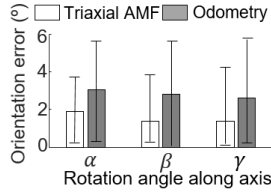


Fig. 27. Orientation error of the path.

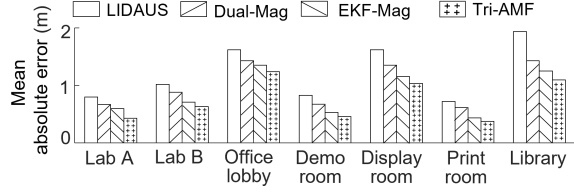


Fig. 28. Mapping performances of different 3D SLAM approaches at various sites.

*Out-trajectory localization:* From the GP-augmented map, during the localization phase, the mobile’s ground-truth trajectory has no crossings with and is within  $3l_k$  from the map trajectory.

*In-trajectory localization performance.* Fig. 23b shows the localization error CDFs of various systems in Lab A. The localization performance trend of these systems is similar to their mapping performance trend shown in Fig. 23a. As the result based on the odometry has much larger errors than all the other methods, to better illustrate the performance of the other sensing modalities, we omit the CDF plot of the odometry based method and present its mean error of 6.42 m in the annotation. The triaxial AMF with GP regularization achieves the lowest mean error of 0.93 m. The mean localization errors based on Wi-Fi and GMF are 3.80 m and 1.62 m. Thus, the triaxial AMF with GP regularization outperforms Wi-Fi and GMF by 75.5% and 42.6%, respectively. The mean error achieved by the uniaxial AMF without GP regularization is 1.36 m, which is slightly better than the 1.59 m in-trajectory localization mean error achieved by the prior work [28] in a lab space. Thus, the triaxial AMF with GP regularization is 31.6% better than that of the uniaxial AMF without GP regularization in terms of the mean localization error. More results at different sites are shown in Fig. 24b. The median errors achieved by triaxial AMF with GP regularization at the eight sites are 0.91 m, 1.74 m, 2.87 m, 1.42 m, 1.78 m, 0.94 m, 3.27 m, and 3.03 m. In short, the triaxial AMF-based GP-assisted SLAM achieves sub-1m to 3m localization errors. At all sites, the triaxial AMF with GP regularization outperforms the uniaxial AMF. The localization errors show a similar advancement pattern as the mapping errors in Fig. 24a, where the improvements are more apparent in the office lobby, car park, and library.

*Performance of partially in-trajectory and out-trajectory localization.* At each site, we conduct experiments for partially in-trajectory and out-trajectory localization based on (1) the triaxial AMF with GP regularization and augmentation and (2) the uniaxial AMF without GP regularization and augmentation. Fig. 25 shows the error bars of the localization errors of different SLAM systems at all eight sites, where the bar represents the mean localization error and the whiskers represent the maximum and minimum errors. At each site, the minimum errors of all SLAM systems are similar, while the differences can be found in the mean and maximum errors. The out-trajectory localization exhibits the largest mean and maximum errors, whereas the in-trajectory achieves the lowest mean and maximum errors. The triaxial AMF consistently outperforms the uniaxial AMF in each of the partially in-trajectory and out-trajectories scenarios. In particular, in the out-trajectory scenario, the triaxial AMF with GP regularization and augmentation outperforms the uniaxial AMF without GP regularization and augmentation by 30.5% on average in terms of mean localization error across the eight sites. Meanwhile, in both scenarios, the triaxial AMF based systems show more improvements on mean error in office lobby, car park, and library, which is consistent with the mapping performance trends shown in Fig. 24.

**5.2.4 Orientation sensing performance.** The 6DoF robotic arm carries the triaxial AMF sensor and follows a prescribed path for multiple loops to collect an AMF trace. The sensor orientations are different at the same position in different loops. We take the prescribed orientation as the ground truth and the odometry’s orientation

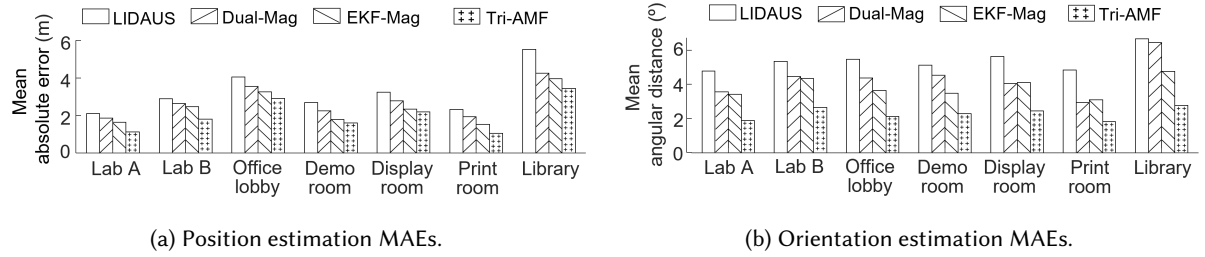


Fig. 29. Localization performances of different 3D SLAM approaches at various sites.

sensing results in the first loop as the base as described in §4.3. Fig. 26 shows the orientation sensing error traces of odometry and our triaxial AMF sensor. The error accumulation problem of odometry can be clearly seen. Differently, the results given by the AMF sensor have stable error distributions over time. Fig. 27 shows the distributions of the orientation sensing errors over the entire experiment, where the bar represents the mean and whiskers represent the minimum and maximum. The AMF sensor achieves sub-2° mean errors in each angular dimension, while the odometry gives larger mean errors.

**5.2.5 Mapping and localization performances comparison of different 3D SLAM approaches.** We conduct experiments at various sites as shown in Fig. 18 to compare the mapping and localization performances of the proposed approach, denoted by Tri-AMF, with three recent 3D SLAM approaches, discussed in §2, where two GMF-based approaches are denoted by EKF-Mag [51] and Dual-Mag [35], and one approach based on Wi-Fi RSS is denoted by LIDAUS [46]. Due to the limitation of implementing the real unmanned aerial vehicle and the drilling machine in indoor environments, the GMF and Wi-Fi RSS data is collected by the built-in IMU and Wi-Fi signal receiver of the smartphone. Noted that to follow the setup of dual magnetic sensors in Dual-Mag, two smartphones of the same type are used for GMF data collection. At each site, the mobile carries the triaxial AMF sensor/smartphone(s) to collect the mapping and localization data following the same trajectory. The mapping performance evaluation focuses on the deviation of the reconstructed 3D map from the ground truth. The localization performance considers the estimation errors in both position and orientation. To have a straightforward view of the localization error in 3D space, we use Euclidean distance and the angular distance [20] to measure the position and orientation difference between the estimation and ground truth, respectively. Fig. 28 shows the bar chart of mapping errors of different SLAM approaches at various sites, where each bar represents the mean absolute error (MAE) of the mapping error. It can be found that all approaches perform better at the smaller-scale sites. Across all sites, Tri-AMF always outperforms with the lowest MAEs. We compare the in-trajectory localization performances of these approaches by calculating the MAEs of position and orientation estimations at each site and illustrate the results in Fig. 29. We can see that both the postion and orientation estimation performances follow the trend of mapping performance in Fig. 28. Benefiting from its more reliable map, Tri-AMF can make more accurate position and orientation estimations than the other approaches at each site. Therefore, better mapping and localization results can be expected by employing the proposed Tri-AMF approach.

## 6 DISCUSSION

In this section, we introduce two mobile platforms for powerline AMF sensing and discuss several other use cases of the AMF sensor which worth further exploration in future work.

## 6.1 Mobile Platforms for Powerline AMF Sensing

In our implementation, the triaxial AMF sensor is integrated with a terrestrial mobile platform to collect the powerline AMF signals in 3D indoor environments. This mobile platform is customized for general indoor sensing tasks as shown in Fig. 18. In addition to ground-based sensing with a terrestrial mobile platform, the use of unmanned aerial vehicles (UAVs) enables free space sensing, which has found wide applications such as monitoring, mapping, and surveying. In a recent work [26], a magnetic field sensor is housed by a customized case installed under a UAV for magnetic field mapping in the indoor environment. When integrating the AMF sensor on a UAV, certain specifics need to be considered. For instance, the measurements in [52] show that the permanent magnet synchronous motor of the UAV can generate three magnetic interference signals. One of them has a frequency of about 50 Hz which is similar to the mains frequency captured by the AMF sensor. Thus, a sufficient separation distance between the sensor and UAV needs to be determined to avoid the interference from the UAV's motor [52, 61].

## 6.2 Other Applications of AMF Sensing

This paper applies triaxial AMF sensing for 3D SLAM and indoor localization. Moreover, the triaxial AMF sensing can enable a broader range of applications, including interior layout planning, public health assessments, and power infrastructure monitoring. We discuss several other possible use cases of the triaxial AMF sensor. First, the triaxial AMF sensing helps generate detailed maps of the AMF distribution in indoor environments influenced by powerlines. These maps are crucial for facility layout planning and public health considerations, because they facilitate the identification of zones with unsafely high AMF intensities. For example, in the medical domain, the presence of 50 Hz/60 Hz electromagnetic radiation and its harmonics can disrupt biopotential recordings [9]. Using the powerline AMF intensity map, such medical examinations can be arranged in areas exhibiting minimal AMF interference, thereby yielding more precise diagnostic outcomes. Second, in the domain of daily healthcare, human AMF exposure is gaining increasing attention due to the reported negative health impacts of powerline AMF [21, 33]. Studies [6, 60] have shown the association between cancer occurrence and prolonged powerline AMF exposure. A recent work [37] uses a uniaxial AMF sensor to assess AMF exposure of primary school students in different classrooms. As the triaxial AMF sensor is more precise and informative, its improved sensing results will be more reliable in determining the human AMF exposure level. Third, using triaxial AMF sensors enables engineers and utility companies to monitor the powerline transmission status. By detecting abnormal AMF patterns, the triaxial AMF based monitoring may provide early indication of equipment malfunctions. As triaxial AMF sensing shows more advantages over uniaxial AMF sensing, in future work, it is interesting to study triaxial AMF sensing for the above applications.

## 7 CONCLUSION

This paper studies an orientation-aware 3D SLAM in AMF, a 3D vector field of low-frequency magnetism induced by powerlines distributed in the indoor space. We design a new resonate antenna-based triaxial AMF sensor to overcome the susceptibility of the existing uniaxial AMF sensor to orientation variations. In addition, to better cope with the high spatial variability of AMF, we design a GP-assisted SLAM algorithm that constructs the GP-augmented AMF map characterizing the proximity of the explored trajectory. Extensive experiments in eight indoor environments show that the proposed GP-assisted triaxial AMF SLAM system achieves sub-1m to 3m median localization errors and outperforms the systems based on Wi-Fi RSS and geomagnetism by 75.5% and 42.6%. It also outperforms the uniaxial AMF SLAM system by 31.6% and 30.5% in the absence and presence of trajectory deviations.

## ACKNOWLEDGMENTS

This study is supported in part under the RIE2020 Industry Alignment Fund – Industry Collaboration Projects (IAF-ICP) Funding Initiative, as well as cash and in-kind contribution from Singapore Telecommunications Limited (Singtel), through Singtel Cognitive and Artificial Intelligence Lab for Enterprises (SCALE@NTU), and in part by Singapore MOE Tier 1(RT14/22).

## REFERENCES

- [1] Aditya Arun, Roshan Ayyalasomayajula, William Hunter, and Dinesh Bharadia. 2022. P2SLAM: Bearing Based WiFi SLAM for Indoor Robots. *IEEE Robotics and Automation Letters* 7, 2 (2022), 3326–3333.
- [2] Roshan Ayyalasomayajula, Aditya Arun, Chenfeng Wu, Sanatan Sharma, Abhishek Rajkumar Sethi, Deepak Vasisht, and Dinesh Bharadia. 2020. Deep learning based wireless localization for indoor navigation. In *Proceedings of the 26th Annual International Conference on Mobile Computing and Networking*. 1–14.
- [3] Anahid Basiri, Elena Simona Lohan, Terry Moore, Adam Winstanley, Pekka Peltola, Chris Hill, Pouria Amirian, and Pedro Figueiredo e Silva. 2017. Indoor location based services challenges, requirements and usability of current solutions. *Computer Science Review* 24 (2017), 1–12.
- [4] Mordechai Ben-Ari and Francesco Mondada. 2018. Robotic motion and odometry. In *Elements of Robotics*. Springer, 63–93.
- [5] José Luis Blanco-Claraco. 2021. A tutorial on SE(3) transformation parameterizations and on-manifold optimization. *arXiv preprint arXiv:2103.15980* (2021).
- [6] David O Carpenter. 2019. Extremely low frequency electromagnetic fields and cancer: How source of funding affects results. *Environmental research* 178 (2019), 108688.
- [7] Douglas Cline. 2017. *Variational principles in classical mechanics*. University of Rochester River Campus Librarie.
- [8] Gabe Cohn, Sidhant Gupta, Tien-Jui Lee, Dan Morris, Joshua R Smith, Matthew S Reynolds, Desney S Tan, and Shwetak N Patel. 2012. An ultra-low-power human body motion sensor using static electric field sensing. In *Proceedings of the 2012 ACM Conference on Ubiquitous Computing (Ubicomp)*. 99–102.
- [9] Tarälungă Dragoș Daniel and Mihaela Neagu. 2018. Cancelling harmonic power line interference in biopotentials. *Compendium of New Techniques in Harmonic Analysis; IntechOpen: London, UK* (2018), 19.
- [10] Jianyang Ding, Yong Wang, Hongyan Si, Shang Gao, and Jiwei Xing. 2022. Three-dimensional indoor localization and tracking for mobile target based on wifi sensing. *IEEE Internet of Things Journal* 9, 21 (2022), 21687–21701.
- [11] D. Droesel and S. Behnke. 2018. Efficient continuous-time SLAM for 3D lidar-based online mapping. In *Proceedings of 2018 IEEE International Conference on Robotics and Automation (ICRA)*. IEEE, 5000–5007.
- [12] Christine Evers and Patrick A Naylor. 2018. Acoustic slam. *IEEE/ACM Transactions on Audio, Speech, and Language Processing* 26, 9 (2018), 1484–1498.
- [13] Brian Ferris, Dieter Fox, and Neil D Lawrence. 2007. Wifi-slam using gaussian process latent variable models. In *Proceedings of the 20th International Joint Conference on Artificial Intelligence (IJCAI)*, Vol. 7. 2480–2485.
- [14] Giorgio Grisetti, Rainer Kümmerle, Cyrill Stachniss, and Wolfram Burgard. 2010. A tutorial on graph-based SLAM. *IEEE Intelligent Transportation Systems Magazine* 2, 4 (2010), 31–43.
- [15] Tobias Grosse-Puppeldahl, Xavier Dellangnol, Christian Hatzfeld, Biying Fu, Mario Kupnik, Arjan Kuijper, Matthias R Hastall, James Scott, and Marco Gruteser. 2016. Platypus: Indoor localization and identification through sensing of electric potential changes in human bodies. In *Proceedings of the 14th Annual International Conference on Mobile Systems, Applications, and Services (MobiSys)*. 17–30.
- [16] Brian Ferris, Dirk Hähnel, and Dieter Fox. 2006. Gaussian processes for signal strength-based location estimation. In *Proceeding of Robotics: Science and Systems*. Citeseer.
- [17] Zakieh S Hashemifar, Charuvahan Adhivarahan, Anand Balakrishnan, and Karthik Dantu. 2019. Augmenting visual SLAM with Wi-Fi sensing for indoor applications. *Autonomous Robots* 43 (2019), 2245–2260.
- [18] DM Henderson. 1977. *Shuttle Program. Euler angles, quaternions, and transformation matrices working relationships*. Technical Report. NASA.
- [19] Joseph Huang, David Millman, Morgan Quigley, David Stavens, Sebastian Thrun, and Alok Aggarwal. 2011. Efficient, generalized indoor wifi graphslam. In *Proceedings of 2011 IEEE International Conference on Robotics and Automation (ICRA)*. IEEE, 1038–1043.
- [20] Du Q Huynh. 2009. Metrics for 3D rotations: Comparison and analysis. *Journal of Mathematical Imaging and Vision* 35 (2009), 155–164.
- [21] Hamed Jalilian, Saeed Hosseini Teshnizi, Martin Röösli, and Masoud Neghab. 2018. Occupational exposure to extremely low frequency magnetic fields and risk of Alzheimer disease: a systematic review and meta-analysis. *Neurotoxicology* 69 (2018), 242–252.
- [22] Manon Kok and Arno Solin. 2018. Scalable magnetic field SLAM in 3D using Gaussian process maps. In *Proceedings of 2018 21st International Conference on Information Fusion (FUSION)*. IEEE, 1353–1360.

- [23] Swarun Suresh Kumar, Stephanie Gil, Dina Katabi, and Daniela Rus. 2018. Indoor localization of a multi-antenna receiver. US Patent 9,885,774.
- [24] Donghwan Lee, Soohyun Ryu, Suyong Yeon, Yonghan Lee, Deokhwa Kim, Cheolho Han, Yohann Cabon, Philippe Weinzaepfel, Nicolas Guérin, Gabriela Csurka, et al. 2021. Large-scale localization datasets in crowded indoor spaces. In *Proceedings of the IEEE/CVF Conference on Computer Vision and Pattern Recognition*. 3227–3236.
- [25] Yang Li, Rui Tan, and David KY Yau. 2018. Natural timestamps in powerline electromagnetic radiation. *ACM Transactions on Sensor Networks (TOSN)* 14, 2 (2018), 1–30.
- [26] Pavol Lipovský, Katarína Draganová, Jozef Novotnák, Zoltán Szöke, and Martin Fil'ko. 2021. Indoor mapping of magnetic fields using uav equipped with fluxgate magnetometer. *Sensors* 21, 12 (2021), 4191.
- [27] Lisandro Lovisolo, Fernando Cruz-Roldán, and Manuel Blanco-Velasco. 2022. On Power Line Positioning Systems. *Sensors* 22, 20 (2022), 7827.
- [28] Chris Xiaoxuan Lu, Yang Li, Peijun Zhao, Changhao Chen, Linhai Xie, Hongkai Wen, Rui Tan, and Niki Trigoni. 2018. Simultaneous localization and mapping with power network electromagnetic field. In *Proceedings of the 24th annual International Conference on Mobile Computing and Networking (MobiCom)*. 607–622.
- [29] Andréa Macario Barros, Maugan Michel, Yoann Moline, Gwenolé Corre, and Frédéric Carrel. 2022. A comprehensive survey of visual slam algorithms. *Robotics* 11, 1 (2022), 24.
- [30] Jan Willem Marck, Ali Mohamoud, Eric vd Houwen, and Rob van Heijster. 2013. Indoor radar slam a radar application for vision and gps denied environments. In *Proceedings of 2013 European Radar Conference*. IEEE, 471–474.
- [31] Christopher G Mouron. 1996. *The first fundamental theorem of invariant theory for the unimodular and orthogonal groups*. Ph.D. Dissertation. Texas Tech University.
- [32] National Institute of Environmental Health Sciences, National Institutes of Health, et al. 2002. Electric and magnetic fields associated with the use of electric power. *NIEHS/DOE EMF RAPID Program* (2002).
- [33] IARC Working Group on the Evaluation of Carcinogenic Risks to Humans, World Health Organization, and International Agency for Research on Cancer. 2002. Non-ionizing Radiation: Static and extremely low-frequency (ELF) electric and magnetic fields. (2002).
- [34] Guanglie Ouyang and Karim Abed-Meraim. 2022. A Survey of Magnetic-Field-Based Indoor Localization. *Electronics* 11, 6 (2022), 864.
- [35] Byeolteo Park and Hyun Myung. 2014. Underground localization using dual magnetic field sequence measurement and pose graph SLAM for directional drilling. *Measurement Science and Technology* 25, 12 (2014), 125101.
- [36] Byeolteo Park and Hyun Myung. 2018. Resilient underground localization using magnetic field anomalies for drilling environment. *IEEE TRANSACTIONS ON INDUSTRIAL ELECTRONICS* 65, 2 (2018), 1377–1387.
- [37] JinKyung Park, EunHye Jeong, and GyeongAe Seomun. 2020. Extremely low-frequency magnetic fields exposure measurement during lessons in elementary schools. *International journal of environmental research and public health* 17, 15 (2020), 5284.
- [38] Shwetak N Patel, Khai N Truong, and Gregory D Abowd. 2006. Powerline positioning: A practical sub-room-level indoor location system for domestic use. In *Proceedings of International Conference on Ubiquitous Computing (Ubicomp)*. Springer, 441–458.
- [39] PCE Instruments. 2022. Electromagnetic field radiation detector PCE-G28. [https://www.pce-instruments.com/english/api/getartfile?fnr=1548022&\\_dsp=inline](https://www.pce-instruments.com/english/api/getartfile?fnr=1548022&_dsp=inline).
- [40] Ananth Ranganathan. 2004. The levenberg-marquardt algorithm. *Tutorial on LM algorithm* 11, 1 (2004), 101–110.
- [41] Anthony Rowe, Vikram Gupta, and Ragunathan Rajkumar. 2009. Low-power clock synchronization using electromagnetic energy radiating from ac power lines. In *Proceedings of the 7th ACM Conference on Embedded Networked Sensor Systems (SenSys)*. 211–224.
- [42] Jianyuan Ruan, Bo Li, Yingqiang Wang, and Zhou Fang. 2020. GP-SLAM+: real-time 3D lidar SLAM based on improved regionalized Gaussian process map reconstruction. In *Proceedings of 2020 IEEE/RSJ International Conference on Intelligent Robots and Systems (IROS)*. IEEE, 5171–5178.
- [43] Matthias Seeger. 2004. Gaussian processes for machine learning. *International journal of neural systems* 14, 02 (2004), 69–106.
- [44] Arno Solin, Manon Kok, Niklas Wahlström, Thomas B Schön, and Simo Särkkä. 2018. Modeling and interpolation of the ambient magnetic field by Gaussian processes. *IEEE Transactions on Robotics* 34, 4 (2018), 1112–1127.
- [45] Erich P Stuntebeck, Shwetak N Patel, Thomas Robertson, Matthew S Reynolds, and Gregory D Abowd. 2008. Wideband powerline positioning for indoor localization. In *Proceedings of the 10th International Conference on Ubiquitous computing (Ubicomp)*. 94–103.
- [46] Yue Sun, Deqiang Xu, Zhuoming Huang, Honggang Zhang, and Xiaohui Liang. 2020. Lidaus: Localization of iot device via anchor uav slam. In *2020 IEEE 39th International Performance Computing and Communications Conference (IPCCC)*. IEEE, 1–11.
- [47] Sebastian Thrun. 2002. Probabilistic robotics. *Commun. ACM* 45, 3 (2002), 52–57.
- [48] Stijn Van Dongen and Anton J Enright. 2012. Metric distances derived from cosine similarity and Pearson and Spearman correlations. *arXiv preprint arXiv:1208.3145* (2012).
- [49] Pramod K Varshney. 2012. *Distributed detection and data fusion*. Springer Science & Business Media.
- [50] Deepak Vasisht, Swarun Kumar, and Dina Katabi. 2016. Decimeter-Level localization with a single Wi-Fi access point. In *13th USENIX Symposium on Networked Systems Design and Implementation (NSDI 16)*. 165–178.

- [51] Frida Viset, Rudy Helmons, and Manon Kok. 2022. An Extended Kalman Filter for Magnetic Field SLAM Using Gaussian Process Regression. *Sensors* 22, 8 (2022), 2833.
- [52] Callum Walter, Alexander Braun, and Georgia Fotopoulos. 2021. Characterizing electromagnetic interference signals for unmanned aerial vehicle geophysical surveys. *Geophysics* 86, 6 (2021), J21–J32.
- [53] Sen Wang, Hongkai Wen, Ronald Clark, and Niki Trigoni. 2016. Keyframe based large-scale indoor localisation using geomagnetic field and motion pattern. In *Proceedings of 2016 IEEE/RSJ International Conference on Intelligent Robots and Systems (IROS)*. IEEE, 1910–1917.
- [54] Chenshu Wu, Feng Zhang, Beibei Wang, and KJ Ray Liu. 2019. EasiTrack: Decimeter-level indoor tracking with graph-based particle filtering. *IEEE Internet of Things Journal* 7, 3 (2019), 2397–2411.
- [55] Zhenyu Yan, Yang Li, Rui Tan, and Jun Huang. 2017. Application-layer clock synchronization for wearables using skin electric potentials induced by powerline radiation. In *Proceedings of the 15th ACM Conference on Embedded Network Sensor Systems (SenSys)*. 1–14.
- [56] Zhenyu Yan, Qun Song, Rui Tan, Yang Li, and Adams Wai Kin Kong. 2019. Towards touch-to-access device authentication using induced body electric potentials. In *Proceedings of The 25th Annual International Conference on Mobile Computing and Networking (MobiCom)*. 1–16.
- [57] Zheng Yang, Zimu Zhou, and Yunhao Liu. 2013. From RSSI to CSI: Indoor localization via channel response. *ACM Computing Surveys (CSUR)* 46, 2 (2013), 1–32.
- [58] Muhammad Salman Yousuf and Mustafa El-Shafei. 2007. Power line communications: an overview-part I. *2007 Innovations in Information Technologies* (2007), 218–222.
- [59] Junbo Zhang, Elahe Soltanaghai, Artur Balanuta, Reese Grimsley, Swarun Kumar, and Anthony Rowe. 2022. PLatter: On the Feasibility of Building-scale Power Line Backscatter. In *Proceedings of 19th USENIX Symposium on Networked Systems Design and Implementation (NSDI)*. 897–911.
- [60] Yemao Zhang, Jinsheng Lai, Guoran Ruan, Chen Chen, and Dao Wen Wang. 2016. Meta-analysis of extremely low frequency electromagnetic fields and cancer risk: a pooled analysis of epidemiologic studies. *Environment international* 88 (2016), 36–43.
- [61] Yaoxin Zheng, Shiyan Li, Kang Xing, and Xiaojuan Zhang. 2021. Unmanned aerial vehicles for magnetic surveys: A review on platform selection and interference suppression. *Drones* 5, 3 (2021), 93.